Zircon U–Pb ages and petrogenesis of late Miocene adakitic rocks from the Sari Gunay gold deposit, NW Iran

Hossein Shahbazi[1] [ORCID], Yasaman Taheri Maghami[1], Hossein Azizi[2],

Yoshihiro Asahara[3], Wolfgang Siebel[4], Mohammad Maanijou[1] and Ali Rezai[1]

[1]Department of Geology, Faculty of sciences, Bu-Ali Sina University, Hamedan, Iran; [2]Department of Mining Engineering, Faculty of Engineering, University of Kurdistan, Sanandaj, Iran; [3]Department of Earth and Environmental Sciences, Graduate School of Environmental Studies, Nagoya University, Nagoya 464-8601, Japan and [4]Institute of Earth and Environmental Sciences, Albert-Ludwig University Freiburg, Freiburg 79104, Germany

Abstract

Late Miocene volcanic rocks host the Sari Gunay epithermal gold deposit in NW Iran. These rocks are located within the Hamedan–Tabriz volcanic belt and occupy the northwestern part of the Sanandaj–Sirjan zone (SaSZ). The volcanic rocks span in composition from latite to dacite and rhyolite. Plagioclase, hornblende, biotite and quartz are the main phenocrysts in a fine-grained and glassy matrix. Laser ablation inductively coupled plasma mass spectrometry zircon U–Pb dating yielded crystallization ages of 10.10 ± 0.01 Ma and 11.18 ± 0.14 Ma for rhyolite and dacite, respectively. High ratios of Sr/Y (> 20) and La/Yb (> 20), high contents of Sr (≥ 400 ppm), low contents of MgO (≤ 6 wt%), Y ≤ 18 ppm (*c.* 16.5 ppm), Yb ≤ 1.9 ppm (*c.* 1.53 ppm) and weak negative Eu anomalies (Eu*/Eu *c.* 0.81) are compatible with a high-silica adakitic signature of the rocks. Regarding the location of the study area nearly 100 km from the Zagros suture zone, we argue that delamination of lithospheric mantle beneath the SaSZ has played a key role in the development of the adakitic rocks in a post-collision tectonic regime. The adakitic melts are suggested to have formed by partial melting of delaminated continental lithosphere and/or lower crustal amphibolite following the collision of the Arabian and Iranian plates.

1. Introduction

Defant & Drummond (1990) first used the term adakite for a group of rocks with high Sr/Y (> 20) and La/Yb (> 20) ratios; high SiO_2 (≥ 56 wt%) and Al_2O_3 (≥ 15 wt%) contents; low MgO (≤ 6 wt%), Y (≤ 18 ppm) and Yb (≤ 1.8 ppm) contents; and low $^{87}Sr/^{86}Sr$ ratios (< 0.7040) without remarkable negative Eu anomaly. Adakitic rocks are widely distributed across the Sanandaj–Sirjan zone (SaSZ) and the Urumieh–Dokhtar Magmatic Arc (UDMA) (Fig. 1). A growing body of research has shown that most adakitic magmas in Iran formed by direct melting of the subducted oceanic slab (Fig. 1), such as post-collisional late Miocene adakitic dacites to rhyodacites in north Tabriz, NW Iran (Jahangiri, 2007); late Miocene and Quaternary adakitic andesites at Salafchegan and Anar area, central UDMA (Omrani *et al.* 2008); Eocene adakitic andesites at Tafresh area (Ghorbani & Bezenjani, 2011); the Paleocene Bibi–Maryam adakitic pluton at Sistan, 40 km NE of Nehbandan (Delavari *et al.* 2014); Cretaceous–Eocene plutonic and volcanic adakitic rocks in the Sabzevar zone (Fig. 1), NE Iran (Omrani, 2018); late Paleocene adakitic felsic intrusions of the Sabzevar zone (Rossetti *et al.* 2014); Eocene intermediate to felsic intrusive and volcanic adakitic rocks at the Sabzevar zone (Shafaii Moghadam *et al.* 2016); and Eocene adakitic rhyolites to andesites of the Sabzevar zone (Jamshidi *et al.* 2018).

A few adakitic rocks in Iran were regarded as products of different magmatic processes. For example, the middle Miocene adakitic quartz diorite, granodiorite and diorite stocks of the Meiduk and Parkam porphyry copper deposits (NE of Shahr-e-Babak) are considered to be derived from melting of thickened continental crust and lithospheric mantle (Alirezaei *et al.* 2017) (Fig. 1). In addition, Miocene intermediate to acidic volcanic adakitic rocks of the Sheyda Volcano in the Ghorveh area (SaSZ and NW Iran) originated from melting of metasomatized continental lithosphere (Torkian *et al.* 2019) (Fig. 1). Cenozoic calc-alkaline adakite-like magmas of the Arasbaran belt (Fig. 1) originated from partial melting of peridotites, while Neogene magmas of this belt were generated by partial melting of garnet-bearing hydrous amphibolite at the lower crust (Jamali & Mehrabi, 2015). Furthermore, the adakites in the northern SaSZ originated from melting of the metasomatic mantle wedge above the oceanic
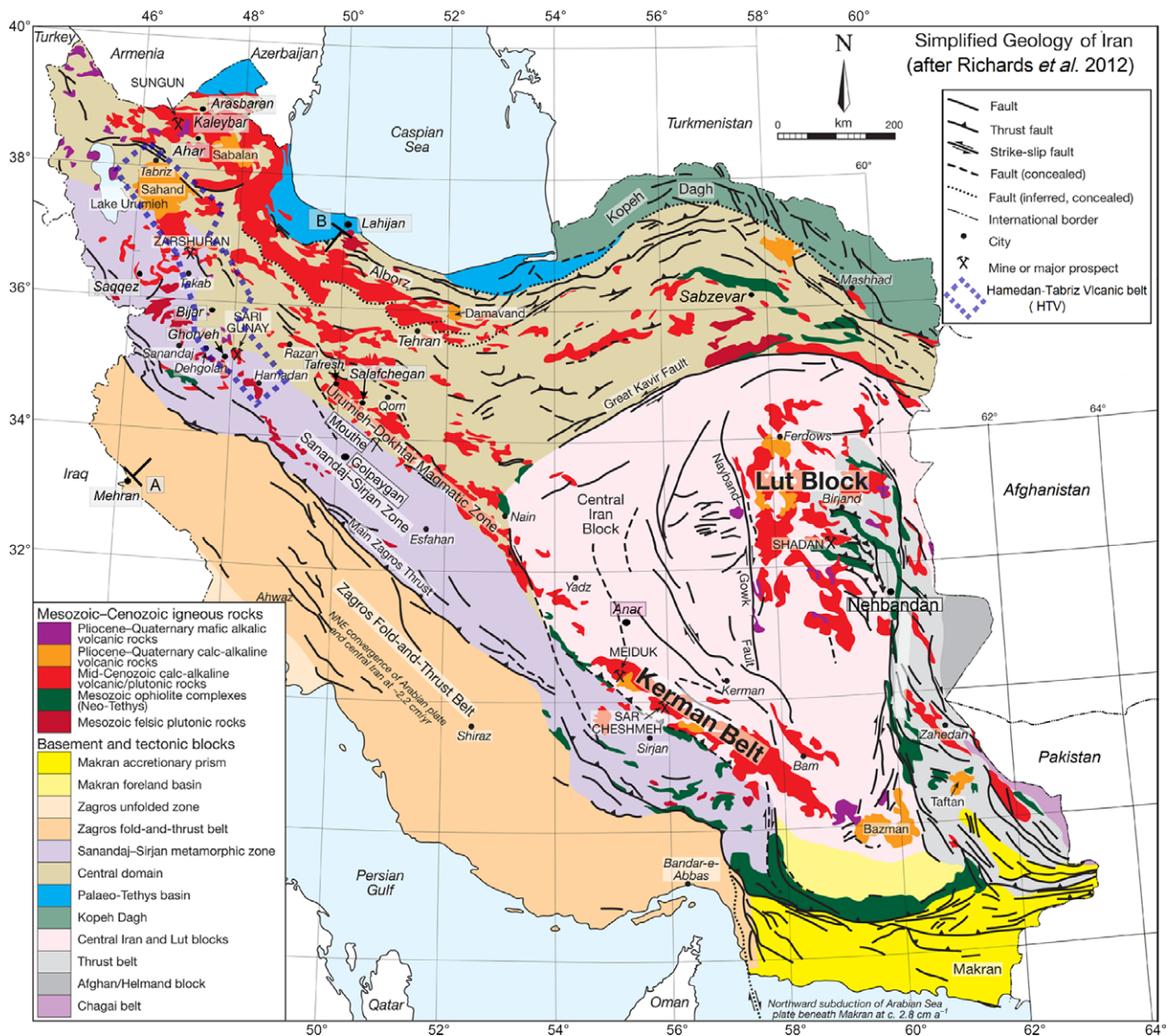
Fig. 1. (Colour online) Simplified geological and tectonic zones of Iran (modified after Richads *et al.* 2012). Location of the Hamedan–Tabriz volcanic belt (HTV) in NW Iran (after Azizi & Moinvaziri, 2009). Location of the Sari Gunay epithermal gold deposit and Moho profile from Mehran to Lahijan (A–B section). Locations with adakitic rocks in Iran mentioned in the text are as follows: Salafchegan (Qom) and Anar (Omrani *et al.* 2008), Tafresh (Ghorbani & Bezenjani, 2011), Ghroveh–Bijar (Azizi *et al.* 2014*a*; Torkian *et al.* 2019), Saqqez–Takab (Azizi *et al.* 2019*a*), Tabriz (Jahangiri, 2007), Arasbaran (Jamali *et al.* 2010; Jamali & Mehrabi 2015), Bibi–Maryam (Nehbandan area) (Delavari *et al.* 2014), Sabzevar area (Rossetti *et al.* 2014; Shafaii Moghadam *et al.* 2016) and Meiduk (Alirezaei *et al.* 2017).

slab, accompanied by minor assimilation of lower mafic calc alkaline continental crust (Azizi *et al.* 2014*a*, 2015).

Numerous researchers have postulated a genetic relation between adakitic melts and the generation of porphyry Cu-Au deposits (Sajona & Maury, 1998; Castillo, 2012; Richards *et al.* 2012; Lohmeier *et al.* 2019). A genetic relationship between adakitic melts and porphyry Cu-Au deposits is well recognized in Iran (Jamali *et al.* 2010; Aghazadeh *et al.* 2011; Asadi *et al.* 2014; Jamali & Mehrabi, 2015; Alirezaei *et al.* 2017). Furthermore, a genetic relation seems to exist between the adakitic volcanic rocks and the Au deposit in the Sari Gunay area, which is the subject of the present study. Here we employ laser ablation inductively coupled plasma mass spectrometry (LA-ICP-MS) zircon U–Pb dating and whole-rock chemical analyses of adakitic rocks from Sari Gunay epithermal gold deposit in the northwestern part of the SaSZ. Based on our new results and previously published studies, we suggest a new geodynamic model for the genesis of the adakitic host rocks and their relation to the Sari Gunay epithermal gold deposit.

2. Geological setting

The Zagros orogen is composed of three parallel NW–SE-trending tectonic zones (Alavi, 1994; Mohajjel *et al.* 2003), namely the Zagros Fold and Thrust Belt, the SaSZ and the Tertiary–Quaternary UDMA (Fig. 1). The orogen formed as a result of Neotethys Ocean closure and the collision between the Arabian and the central Iranian microplates (Dewey *et al.* 1973; Berberian & King, 1981; Alavi, 1994; Hassanzadeh & Wernicke, 2016; Barber *et al.* 2018; Tavakoli *et al.* 2020). The opening of the Neotethys Ocean resulted from rifting of the Cimmerian block (ancient continent including the SaSZ and Central Iran) away from
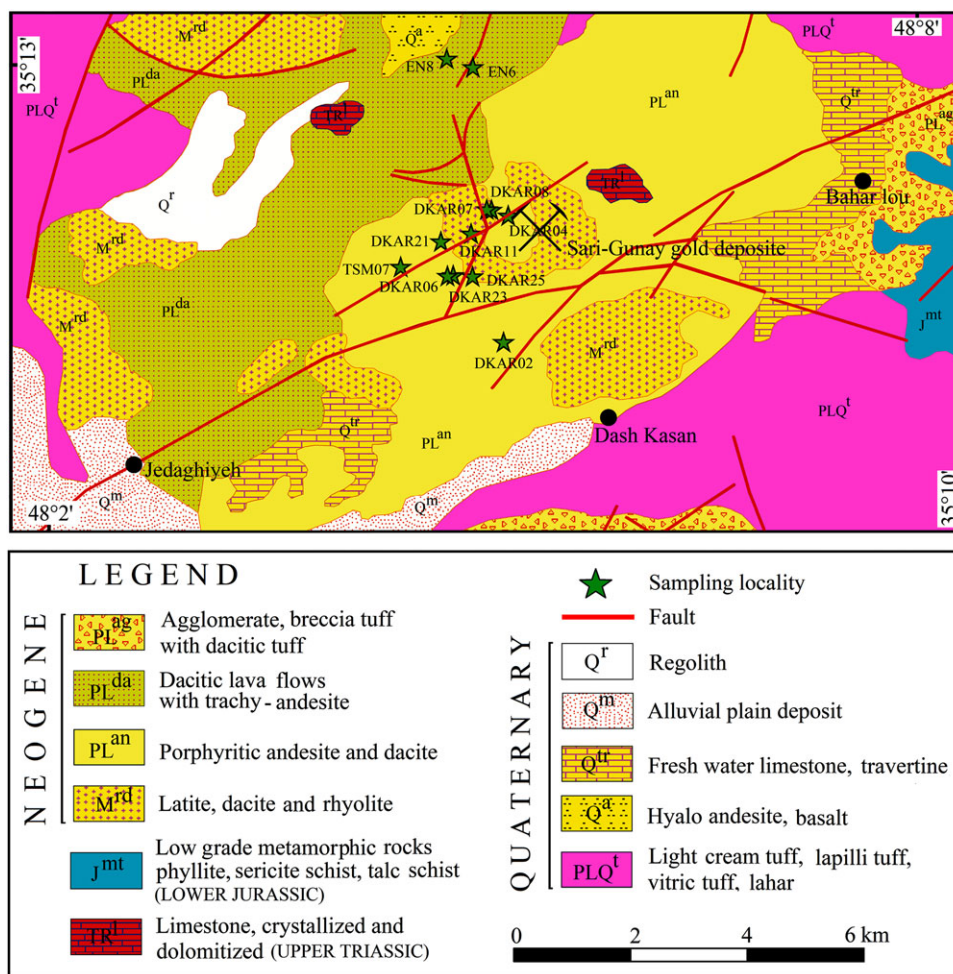
Fig. 2. (Colour online) Geological map of the Sari Gunay epithermal gold deposit area Sanandaj–Sirjan zone (SaSZ), NW Iran, and sampling locality, redrawn from Geological Map of Iran 1:100 000 Series Sheet No. 5660 (Kohin) Geological Survey and Mineral Exploration of Iran (Khan Nazar *et al.* 2015).

the northern margin of Gondwana. The Neotethys oceanic crust started to be subducted beneath Eurasian during Early Jurassic or Late Triassic time (Stampfli & Borel, 2002; Hassanzadeh & Wernicke, 2016). The final closure of the Neotethys and the collision of the Arabian and Eurasia plates occurred during late Oligocene – early Miocene (Berberian *et al.* 1982; Mouthereau *et al.* 2012) and/or early Miocene (Allen *et al.* 2004), early–middle Eocene (Ghasemi & Talbot, 2005), or Late Cretaceous – Oligocene (Mohajjel & Fergusson, 2014) time.

In the study area, the SaSZ basement is composed of Neoproterozoic – early Cambrian biotite–hornblende granodiorite (Hassanzadeh *et al.* 2008). The basement of the SaSZ is also present as crustal xenoliths in the Qezeljeh Kand Plio-Quaternary volcanic cones (Veysi *et al.* 2015) 20 km NW of the Sari Gunay area. Carboniferous – early Permian A-type granitoids, such as the Hasanrobat, Ghushchi and Hasansaralan granites in the Golpaygan area, are associated with the early-stage Neotethys opening (Alirezaei & Hassanzadeh, 2012; Shafaii Moghadam *et al.* 2015; Azizi *et al.* 2017), whereas Middle Jurassic – Early Cretaceous gabbroic to granitoid plutonic rocks are related to the subduction of Neotethys Ocean (Shahbazi *et al.* 2010, 2015; Azizi *et al.* 2011, 2019*a*, *b*). Based on regional geological maps (Khan Nazar *et al.* 2015), Triassic Alisadr Limestone and the Jurassic Hamedan Phyllite are the oldest rocks in the study area (Fig. 2).

The Hamedan–Tabriz Volcanic belt (HTV belt) occupies the NW part of the SaSZ (Fig. 1) and contains extrusive rocks made of ash flows, lava flows, lahars and pyroclastic rocks with massive to flow banding structure. Some Miocene volcanic rocks in the HTV belt have adakitic features (Jahangiri, 2007; Azizi *et al.* 2014*a*, *b*; Lechmann *et al.* 2018; Torkian *et al.* 2019). The southern HTV belt (Ghorveh and Bijar area; see Fig. 1) includes two different groups of volcanic rocks. The first group consists of Miocene intermediate to felsic rocks while the second group includes high-Nb Quaternary basaltic rocks (Boccaletti *et al.* 1976; Azizi & Moinevaziri, 2009; Azizi *et al.* 2014*a*, *b*). There are no Eocene volcanic rocks in the HTV belt, while middle Miocene – Plio-Quaternary volcanic rocks are well developed (Azizi & Moinevaziri, 2009).

The Sari Gunay epithermal gold deposit has been investigated in previous studies. Biotite and hornblende ^{40}Ar/^{39}Ar dating (Richards *et al.* 2006) has shown that the host rock of the Sari Gunay deposit formed as a collision-related alkalic-type epithermal system during middle–late Miocene time (Tortonian) at 11.2 Ma (Table 1). Sericite ^{40}Ar/^{39}Ar dating (Richards *et al.* 2006) indicates that sericitic alteration, silicification and Au mineralization happened during a late hydrothermal stage at 10.5 Ma (Table 1). As shown in Table 1, the late Miocene (Tortonian) adakitic rocks at the Sari Gunay gold deposit

Table 1. Summary of K–Ar, ^{40}Ar–^{39}Ar and zircon U–Pb age data of the Miocene volcanic rocks from the Sari Gunay gold deposit and the Ghorveh-Bijar area, Sanandaj–Sirjan zone, NW Iran

Lithology	Method	Age (Ma)	Reference
Ghorveh–Bijar area (north of Akhikamal village)			
Acidic volcanic rocks	Whole-rock K–Ar	8.4 ± 0.2	Boccaletti *et al.* (1976)
		8.6 ± 0.2	
		8.7 ± 0.4	
		8.8 ± 0.2	
		9.2 ± 0.2	
		8.3 ± 0.2	
Sari Gunay gold deposit			
Dacite	Biotite ^{40}Ar–^{39}Ar	11.03 ± 0.16	Richards *et al.* (2006)
Dacite		11.16 ± 0.16	
Trachyte		11.01 ± 0.12	
Rhyolite		11.39 ± 0.07	
Trachyte		11.09 ± 0.10	
Trachyte	Hornblende ^{40}Ar–^{39}Ar	11.69 ± 0.12	
Latite		11.21 ± 0.13	
Sericitized porphyry	Sericite ^{40}Ar–^{39}Ar	10.69 ± 0.10	
Sericitized porphyry		10.27 ± 0.10	
Sericitized porphyry		10.83 ± 0.10	
Ghorveh–Bijar area (north of Akhikamal village)			
Acidic adakitic volcanic rocks	Biotite ^{40}Ar–^{39}Ar	12.3 ± 0.2	Azizi *et al.* (2014*b*)
		10.9 ± 0.1	
		10.6 ± 0.1	
		10.5 ± 0.1	
		10.5 ± 0.1	
		10.5 ± 0.1	
		10.5 ± 0.1	
		10.3 ± 0.2	
		10.2 ± 0.2	
		9.9 ± 0.2	
		10.5 ± 0.4	
		14.8 ± 0.8	
Sari Gunay gold deposit			
Dacite	LA-ICP-MS zircon U–Pb	11.18 ± 0.14	Present study
Rhyolite		10.10 ± 0.01	

formed contemporaneously with adakites in the Ghorveh–Bijar area, such as the Akhikamal volcanic dome with an age of 10.4 Ma, 45 km NW of the Sari Gunay area (Boccaletti *et al.* 1976; Azizi *et al.* 2014*a*). Initial ^{87}Sr/^{86}Sr ratios of the adakites in the Ghorveh–Bijar area are relatively high (0.7070–0.7079) and they depict low $\epsilon(t)_{Nd}$ values between −4 and −2 (Azizi *et al.* 2014*a*). Such isotope features indicate that the rocks were derived from partial melting of lower continental crust and/or a metasomatized lithospheric mantle.

3. Field relations and petrography

3.a. Field relations

In the study area, Miocene volcanic rocks are exposed as part of a composite volcano in the form of small domes consisting of andesite, latite, trachyte, dacite and rhyolite (Fig. 3a–c). The Sari Gunay volcanic complex contains extrusive rocks including ash and lava flows, lahars and pyroclastic rocks with massive to flow banding structure (Fig. 2). The Sari Gunay epithermal gold deposit occurs at a NNE–SSW-
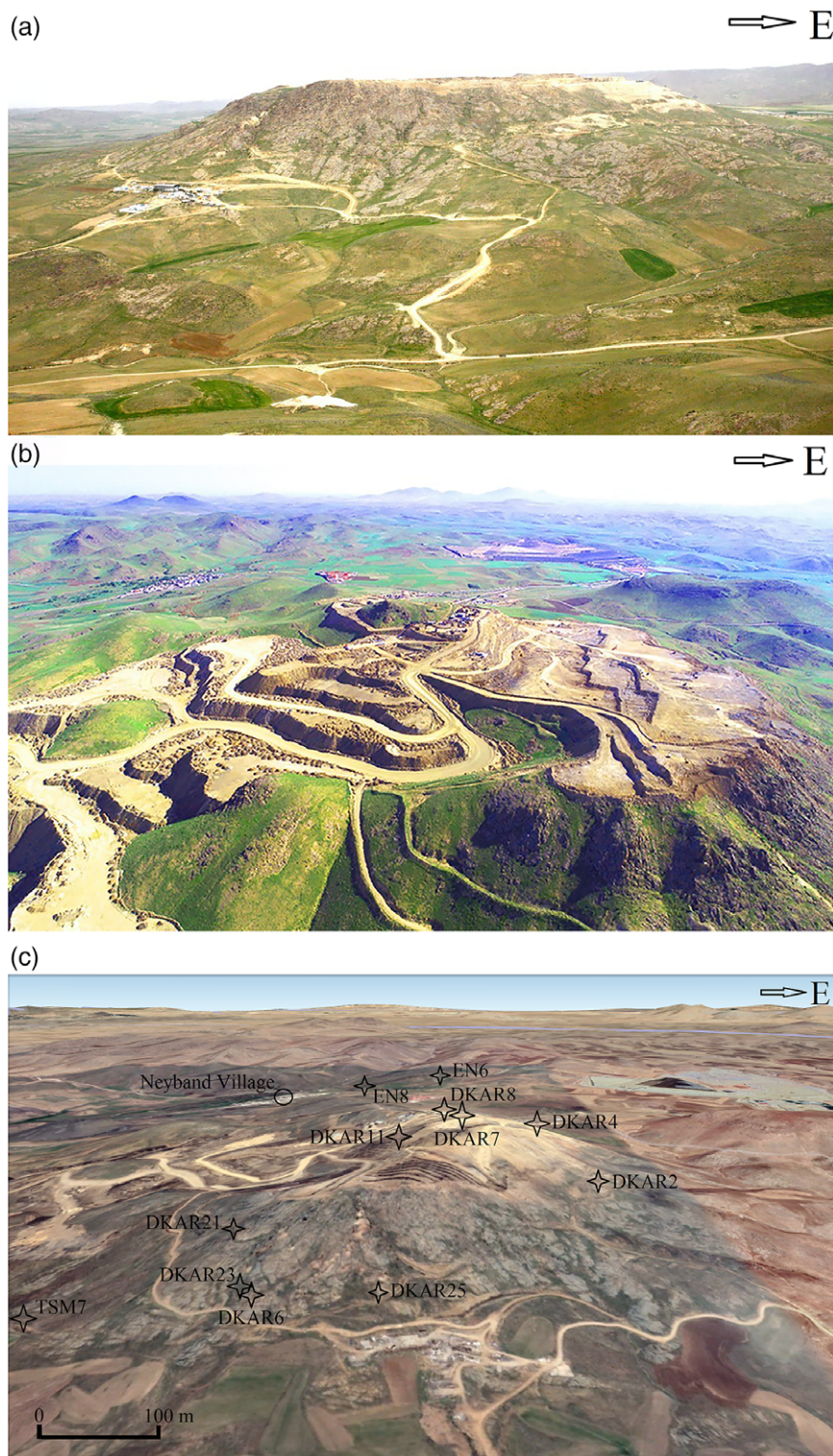
Fig. 3. (Colour online) Field view of the Sari Gunay epithermal gold deposit. (a, b) Field photographs from the hillside of the Sari Gunay epithermal gold deposit. (c) Locations of samples DKAR11 (rhyolite) and DKAR21 (dacite) chosen for U–Pb dating.

trending volcanic hillside, about 1.2 km long and 450 m wide, and extends vertically down at least 300 m (Fig. 4a–c). The deposit consists of a central high-grade mineralized zone, about 75 m wide with a maximum width of 150 m, and two smaller high-grade zones (Wilkinson, 2005). These are in turn surrounded by a low-grade mineralized halo (Fig. 4a–d). Average gold grade is about 2–2.5 g t^{-1} Au in the high-grade mineralized zones and 0.7–0.8 g t^{-1} Au in the lower-grade halo zone.

Based on core logging observations in the Sari Gunay gold deposit, the high-grade zones, represented by tourmaline-quartz breccia units, have formed during hydrothermal alteration associated with silicification. Sericite is also developed in this zone but it has either little or no gold. A weak hypogene copper mineralization is located beneath the main epithermal mineralization and starts about 300 m below the surface. Average grade in this zone is 0.1–0.2% Cu and 0.3–0.6 g t^{-1} Au.
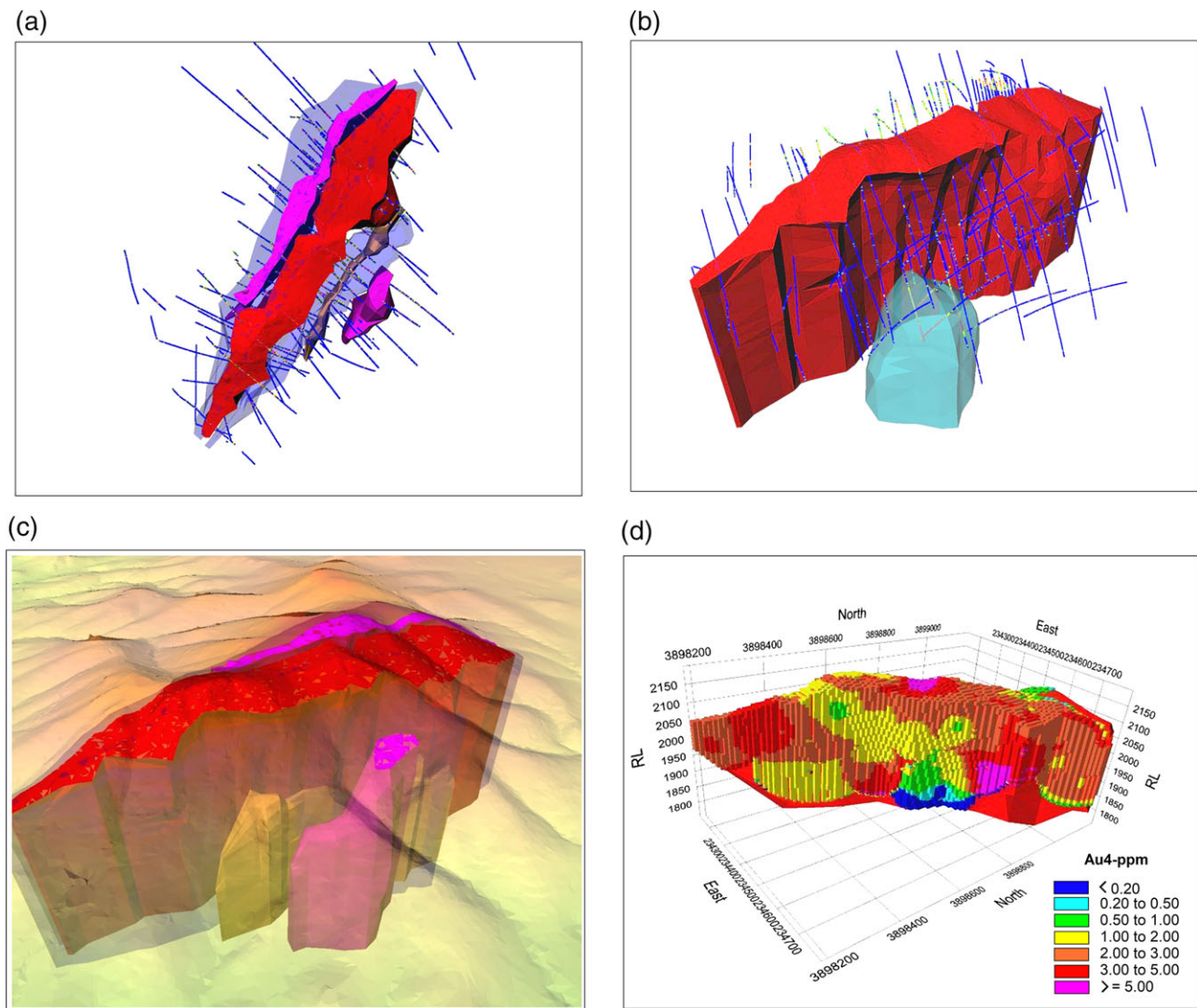
Fig. 4. (Colour online) (a) Plan view of the Sari Gunay gold mine deposit. NW–SE-trending high-grade gold bodies are shown in pink and beige; low-grade gold halo zone shown in light blue and drill-holes lines (blue). (b) 3D view of the high-grade gold ore body (red) Cu-Au, porphyry body (aqua colour), and drill holes lines (blue). (c) Oblique 3D view of Sari Gunay mine with topographic features looking NW. (d) Block model of the central high-grade gold bodies showing gold grade distribution (after Wilkinson, 2005).

Based on a recent study by Graniana *et al.* (2014), the Sari Gunay epithermal gold deposit shows strong vertical and lateral zonation. It is strongly enriched in Au, Sb and Hg in its central part and in As, Pb, Zn and Cu at its margin. Graniana *et al.* (2014) argue that the gold mineralization occurred during two stages: during the first stage, referred to as the sericite alteration phase, gold formed as micro-sized inclusions within pyrite; and during the second stage, the silicification-phase gold formed as a solid solution (invisible gold) within arsenian pyrite.

3.b. Petrography

The volcanic host rocks of the Sari Gunay epithermal gold deposit show some variation ranging from latite, quartz latite to dacite and rhyolite with porphyritic, vitrophyric, trachytic and seriate textures prevailing (Fig. 5). The latites contain plagioclase and K-feldspar phenocrysts in a fine-grained matrix (Fig. 5b, c). Plagioclase phenocrysts are euhedral, show sieve structure in some grains (Fig. 5b) and are 1–2 mm in length (Fig. 5b, c). K-feldspar phenocrysts are present as euhedral to subhedral sanidine, often showing Carlsbad twinning, and are 0.5–1 mm in grain size (Fig. 5c). The quartz latites with porphyritic

and vitrophyric textures mainly comprise plagioclase, volcanic glass, K-feldspar, hornblende, biotite and quartz in some rock varieties (Fig. 5d, e). Phenocryst abundances vary from 30 to 40 vol.% in these rocks. Plagioclase phenocrysts show oscillatory zoning in some grains and are 1–1.5 mm in length. Hornblendes are euhedral to subhedral with oxidized rims, rhomboid in shape, 0.5–2 mm in length and with pleochroism ranging in colour from green to brown (Fig. 5d, e). Biotite occurs as phenocryst, 0.5–1.5 mm in size (Fig. 5d). The dacites have glomeroporphyritic and vitrophyric textures (Fig. 5f–h). Dacites frequently show oscillatory zoning of plagioclase and K-feldspar as euhedral sanidine with Carlsbad twinning, 1–2 mm in grain size; accessory minerals are zircon grains and muscovite (Fig. 5f–h). Hydrothermal alterations, such as sericitization of plagioclase, sanidine and matrix are developed in some dacite varieties (Fig. 5f–h). The rhyolites contain quartz and volcanic glass (Fig. 5i–l). Quartz shows rounded forms and sizes ranging from 0.5 to 2 mm with reaction rims (Fig. 5i). The rock matrix consists of glassy, fine-grained minerals containing quartz, opaque minerals and muscovite. Some pronounced hydrothermal alterations such as silicification (Fig. 5j–l) and tourmalinization with formation of radiated aggregates or small single prisms of tourmaline
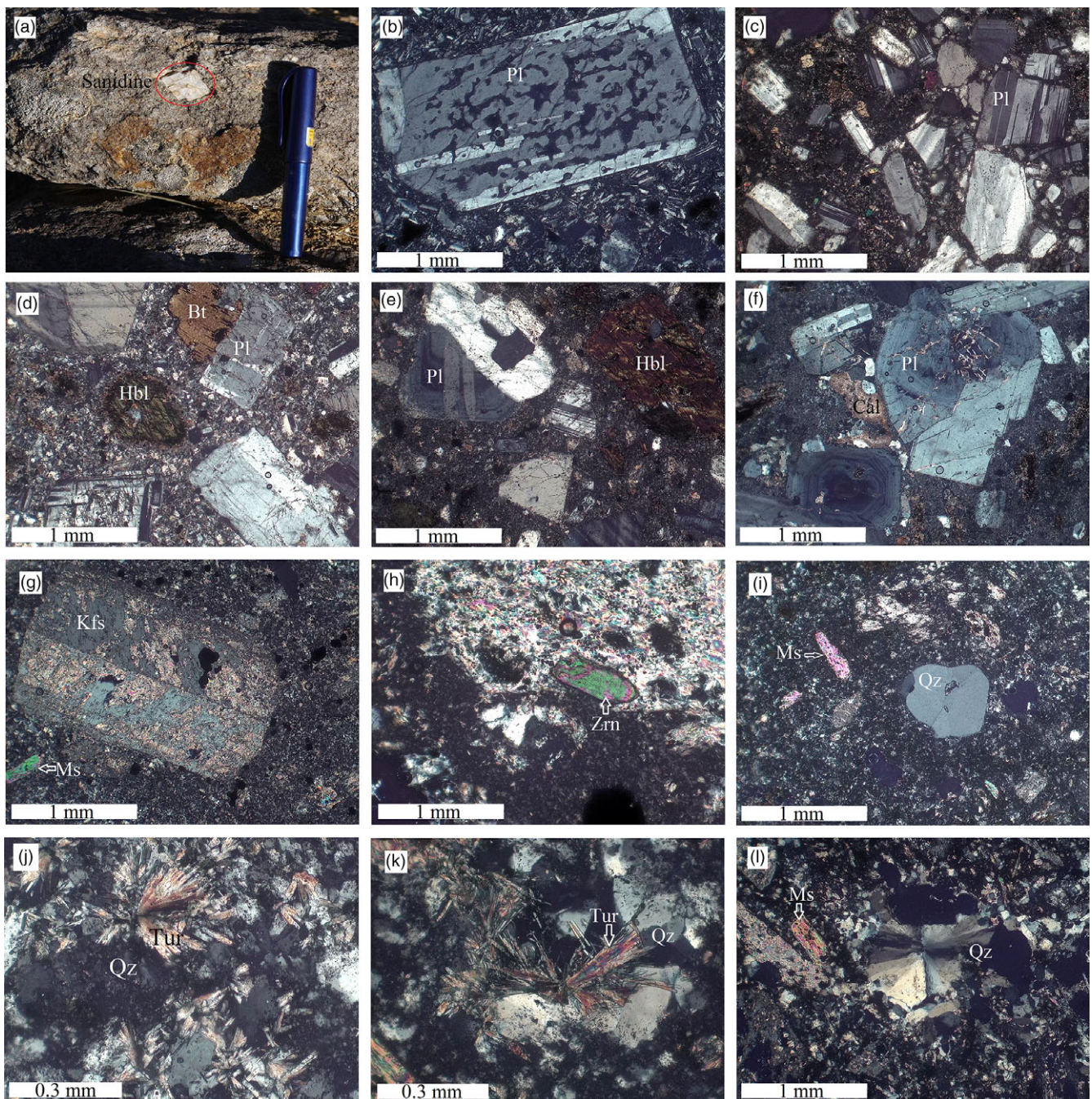
Fig. 5. (Colour online) Field photographs and photomicrographs of adakitic rocks from Sari Gunay: (a) sanidine phenocryst in a dacite; (b) sieve texture of plagioclase phenocryst in latite sample; (c) seriate textures in latite; (d) porphyritic texture, plagioclase, biotite and hornblende phenocrysts set in a quartz latite fine-grained matrix; (e) vitrophyric texture and zoning of plagioclase and hornblende phenocrysts in quartz latite; (f) glomeroporphyritic texture and oscillatory zoning of plagioclase in dacite; (g) sericitized K-feldspar phenocrysts (sanidine) with euhedral shape and Carlsbad twins in a dacite; (h) zircon grain and sericitization and devitrified glass in dacite matrix; (i) quartz phenocrysts in a rhyolite; (j, k) radial euhedral tourmaline aggregates in rhyolites; and (l) silicification relationships in a rhyolite sample. Pl – plagioclase; Hbl – hornblende; Kfs – K-feldspar; Qz – quartz; Ms – muscovite; Tur – tourmaline; Cal – calcite; Zn – zircon (Whitney & Evans, 2010).

usually associated with quartz (Fig. 5j, k) can be observed in the rhyolitic host rocks of Sari Gunay gold deposit.

4. Analytical methods

4.a. Whole-rock analytical procedures

Base on petrographic observation, low- to non-altered samples were collected from different types of the host rock (latite, quartz latite, dacite, rhyolite) of the gold deposit (mineralized zone). Three other samples (quartz latite DKAR02 and dacite EN6, EN8) were selected outside the gold mineralized zone for whole-rock geochemical analyses. The sampling locations are shown in Figures 2 and 3c; rock types and the latitude/longitude of the sample localities are listed in Table 2. Before crushing the samples by a jaw crusher, all their oxidized and altered parts were removed. After powdering in an agate mill, the samples were heated in a high-temperature muffle furnace at 1000°C with lithium borate

Table 2. Major- and trace-element concentrations of the Sari Gunay epithermal gold deposit host rocks

Rock type	Rhyolite					Quartz latite			Latite	Dacite		
Sample	DKAR04	DKAR06	DKAR07	DKAR08	DKAR11	DKAR02	DKAR21	DKAR23	DKAR25	EN6	EN8	TSM07
Longitude (E)	48°05'09''	48°04'47''	48°05'02''	48°05'01''	48°04'54''	48°05'08''	48°04'47''	48°04'47''	48°04'55''	48°04'55''	48°04'46''	48°04'25''
Latitude (N)	35°11'58''	35°11'31''	35°11'59''	35°11'59''	35°11'49''	35°11'47''	35°11'36''	35°11'31''	35°11'31''	35°12'58''	35°12'51''	35°11'35''
SiO_2 (%)	71.21	67.36	66.35	70.23	67.54	61.77	62.34	61.54	57.78	63.7	63.47	65.12
TiO_2	0.38	0.42	0.41	0.44	0.5	0.55	0.58	0.55	0.49	0.54	0.51	0.54
Al_2O_3	12.12	14.42	13.52	14.68	17.39	16.9	16.75	16.4	15.33	16.38	16.41	16.87
Fe_2O_3	4.33	4.09	4.59	2.52	1.74	4.64	5.32	4.67	6.72	2.84	3.92	3.79
MnO	0.02	<0.01	0.01	<0.01	<0.01	0.18	0.13	0.17	0.24	0.08	0.07	0.05
MgO	1.05	0.45	1.04	0.53	0.37	0.97	1.77	2.06	1.61	0.82	1.28	1.37
CaO	0.1	0.09	0.08	0.1	0.28	2.79	3.72	4.04	4.97	5.19	4.36	3.25
Na_2O	0.36	0.19	0.36	0.22	0.22	5.00	5.24	5.32	3.87	4.15	4.38	4.26
K_2O	4.99	9.47	8.02	9.79	10.07	3.76	3.81	3.78	4.54	3.19	3.39	3.2
P_2O_5	0.03	0.20	0.21	0.04	0.11	0.27	0.32	0.28	0.26	0.29	0.28	0.29
LOI	2.81	2.90	4.62	2.93	2.77	2.10	1.70	1.61	3.51	3.86	1.64	2.60
Total	97.50	99.81	99.38	101.69	101.19	99.28	102	100.74	99.60	101.39	100.03	101.65
V (ppm)	81	61	82	67	76	87	101	90	92	68	76	83
Cr	51	105	319	93	46	89	133	101	120	76	83	82
Co	9.6	12.4	0.7	0.4	1.2	11.9	12.2	11	12.5	7.7	8.9	9.7
Ni	10.6	23.7	14	7.2	26	23.3	40.1	28.1	56.2	20.4	20.5	22.6
Ga	15.5	16.1	18.8	19.4	20	19.8	19.2	17.9	17.6	18.3	18.4	19
Sn	17	<5	<5	5	<5	<5	<5	<5	<5	<5	<5	<5
Rb	202.2	356.6	297.9	358.4	394	154.8	134.9	112	138.5	103.6	107.7	101.3
Sr	60.2	118.6	85.9	121.7	129.3	1126	1102.6	1047.6	827.4	1034.1	1038.6	1049.6
Y	13.5	13.8	14.2	13.5	16.2	16.2	14.5	16.7	19.6	23.8	17.4	18.2
Zr	137	122	142	162	210	143	178	161	156	196	187	207
Nb	15.2	17.6	17.3	22.1	20.2	18.7	18.3	17.1	15.7	21	19.6	19.7
Cs	5.15	5.51	3.85	6.06	31.46	4.81	4.88	3.8	7.46	6.81	4.66	5.52
Sc	5.4	5.6	4.3	5.9	5.5	8.8	11.1	11	8.7	7	7.5	8.2
Ba	1027.8	1746.1	1006.6	1568.8	1781.9	1928.9	1687.9	1661	1638.2	1597	1784.7	1726.4
Hf	3.8	3.7	4.1	4.5	5.5	4.2	4.8	4.4	4.2	5.1	5	5.6
Ta	1.2	1.3	1.3	1.5	1.4	1.5	1.3	1.2	1.3	1.4	1.4	1.4
TC	<0.01	<0.01	<0.01	<0.01	0.03	<0.01	0.01	<0.01	0.67	0.48	0.14	0.06

(Continued)

Table 2. (*Continued*)

TS	3.17	3.35	1.27	0.58	0.04	<0.01	<0.01	<0.01	0.15	0.03	<0.01	<0.01
Th	22.77	28.18	23.75	30.04	37.71	31.17	34.18	34.1	31.83	26.5	36.1	33.74
U	6.53	10.78	7.05	13.57	9.58	5.56	5.95	4.83	6.86	8.97	9.18	7.56
W	4	11	5	6	5	4	4	3	2	<1	1	<1
La	25	57.2	56.4	67.8	81.8	77.3	72.7	62.6	57.9	73.6	72.5	62.9
Ce	42.1	92.4	92.3	109.9	132.1	127.7	115	99.8	101.5	122.7	116.6	106.7
Pr	4.55	9.63	9.7	11.6	13.85	12.47	12.18	11.05	11.3	12.46	12.4	11.01
Nd	15.5	30.8	31.2	37.7	45.3	40.8	40.1	37.1	38.8	42.8	41.1	36.5
Sm	2.65	4.49	4.81	5.34	6.91	6.38	6.11	6.38	6.5	7.29	6.72	5.96
Eu	0.56	1.19	0.99	1.15	1.68	1.71	1.62	1.6	1.62	1.7	1.66	1.56
Gd	2.3	3.77	3.96	4.31	5.79	5.35	5.13	5.34	5.48	6.24	5.49	5.03
Tb	0.33	0.42	0.46	0.46	0.64	0.59	0.56	0.61	0.65	0.78	0.63	0.57
Dy	1.95	2.23	2.35	2.13	3.03	3.02	2.67	3.16	3.39	3.94	3.31	3.29
Ho	0.44	0.45	0.46	0.43	0.56	0.57	0.51	0.58	0.66	0.74	0.63	0.65
Er	1.4	1.32	1.42	1.33	1.54	1.65	1.49	1.67	1.84	2.18	1.76	1.83
Tm	0.23	0.21	0.21	0.21	0.23	0.23	0.21	0.26	0.26	0.22	0.26	0.27
Yb	1.45	1.38	1.37	1.42	1.46	1.44	1.29	1.49	1.56	2.01	1.71	1.73
Lu	0.23	0.22	0.22	0.24	0.24	0.23	0.19	0.22	0.25	0.29	0.27	0.26
La/Yb	17.24	41.45	41.17	47.75	56.03	53.68	56.36	42.01	37.12	36.62	42.40	36.36
Sr/Y	4.46	8.59	6.05	9.01	7.98	69.51	76.04	62.73	42.21	43.45	59.69	57.67
Eu/Eu*	0.69	0.88	0.69	0.73	0.81	0.89	0.88	0.84	0.83	0.77	0.83	0.87
(La)N	80.65	184.52	181.94	218.71	263.87	249.35	234.52	201.94	186.77	237.42	233.87	202.9
(Yb)N	6.94	6.6	6.56	6.79	6.99	6.89	6.17	7.13	7.46	9.62	8.18	8.28
(La/Yb)N	11.62	27.96	27.73	32.21	37.75	36.19	38.01	28.32	25.04	24.68	28.59	24.50

Fig. 6. (Colour online) (a) Cathodoluminescence (CL) images of zircons from sample DKAR11 (rhyolite). (b) CL images from zircons of sample DKAR21 (dacite) with positions of ablation.

flux. The fused sample was then cooled and dissolved in dilute nitric acid. Major elements were measured by ICP optical emission spectroscopy (ICP-OES) using a Thermo Scientific/iCAP 6000, while trace elements including the rare earth elements were measured by ICP-MS using Perkin Elmer/NexION 300D. STD OREAS 24b, STD OREAS 45e and STD SY-4 were used as standard samples during the measurement. The detection limits were: 0.01% for major oxides; 0.1 ppm for Ta and Ce; 0.01 ppm for Tb, Tm and Cs; 0.05 ppm for Th and Dy; 0.03 ppm for Er and Yb; 0.5 ppm for Ba; 0.1 ppm for Co and Sc; 0.2 ppm for Ni; and 10 ppm for Cr.

Table 3. U–Pb isotopic data for zircon crystal determined by LA-ICP-MS in volcanic host rocks of the Sari Gunay epithermal gold deposit

Spot	Th/U	$^{207}Pb/^{235}U$	Error (±2σ)	$^{206}Pb/^{238}U$	Error (±2σ)	ρ	$^{235}U–^{207}Pb$ (Ma)	Error (±2σ)	$^{238}U–^{206}Pb$ (Ma)	Error (±2σ)
DK-AR-11 (Rhyolite)										
DK-AR-11-01[a]	0.37	0.13011	0.01393	0.00165	0.00009	0.52	124.2	13.3	10.6	0.6
DK-AR-11-02	0.40	0.01099	0.00282	0.00153	0.00007	0.19	11.1	2.8	9.8	0.5
DK-AR-11-03[a]	0.43	0.01565	0.00297	0.00165	0.00007	0.23	15.8	3.0	10.6	0.5
DK-AR-11-04	0.29	0.00947	0.00272	0.00152	0.00008	0.17	9.6	2.7	9.8	0.5
DK-AR-11-05	0.33	0.01079	0.00236	0.00149	0.00007	0.20	10.9	2.4	9.6	0.4
DK-AR-11-06[a]	0.29	0.01578	0.00386	0.00154	0.00008	0.22	15.9	3.9	9.9	0.5
DK-AR-11-07	0.29	0.00984	0.00245	0.00152	0.00007	0.18	9.9	2.5	9.8	0.4
DK-AR-11-08	0.26	0.00750	0.00272	0.00166	0.00008	0.14	7.6	2.7	10.7	0.5
DK-AR-11-09	0.25	0.00966	0.00231	0.00154	0.00008	0.22	9.8	2.3	9.9	0.5
DK-AR-11-10	0.25	0.01079	0.00213	0.00158	0.00007	0.24	10.9	2.1	10.2	0.5
DK-AR-11-11	0.26	0.01382	0.00229	0.00154	0.00007	0.27	13.9	2.3	9.9	0.5
DK-AR-11-12	0.22	0.01186	0.00238	0.00161	0.00008	0.25	12.0	2.4	10.4	0.5
DK-AR-11-13	0.31	0.01214	0.00258	0.00157	0.00008	0.25	12.3	2.6	10.1	0.5
DK-AR-11-14	0.28	0.01296	0.00278	0.00151	0.00008	0.26	13.1	2.8	9.7	0.5
DK-AR-11-15	0.19	0.01059	0.00185	0.00156	0.00007	0.25	10.7	1.9	10.0	0.4
DK-AR-11-16[a]	0.38	0.02713	0.00433	0.00162	0.00009	0.34	27.2	4.3	10.4	0.6
DK-AR-11-17	0.32	0.01065	0.00299	0.00166	0.00010	0.21	10.8	3.0	10.7	0.6
DK-AR-11-18	0.26	0.01024	0.00197	0.00154	0.00008	0.27	10.3	2.0	9.9	0.5
DK-AR-11-19[a]	0.39	0.01290	0.00323	0.00165	0.00010	0.23	13.0	3.3	10.6	0.6
DK-AR-11-20	0.24	0.00975	0.00345	0.00161	0.00010	0.17	9.9	3.5	10.4	0.6
DK-AR-11-21	0.25	0.00921	0.00226	0.00164	0.00009	0.22	9.3	2.3	10.6	0.6
DK-AR-11-22[a]	0.23	0.01777	0.00164	0.00249	0.00011	0.47	17.9	1.7	16.0	0.7
DK-AR-11-23	0.35	0.01015	0.00276	0.00155	0.00009	0.21	10.3	2.8	10.0	0.6
DK-AR-11-24	0.29	0.00986	0.00314	0.00159	0.00010	0.19	10.0	3.2	10.3	0.6
DK-AR-11-25	0.25	0.00989	0.00244	0.00153	0.00007	0.20	10.0	2.5	9.9	0.5
DK-AR-11-26	0.29	0.00973	0.00253	0.00163	0.00008	0.19	9.8	2.6	10.5	0.5
DK-AR-11-27	0.28	0.01122	0.00230	0.00156	0.00007	0.22	11.3	2.3	10.0	0.4
DK-AR-11-28	0.32	0.01198	0.00254	0.00160	0.00007	0.22	12.1	2.6	10.3	0.5
DK-AR-11-29	0.34	0.01067	0.00358	0.00160	0.00010	0.19	10.8	3.6	10.3	0.6
DK-AR-11-30	0.63	0.01110	0.00247	0.00157	0.00007	0.21	11.2	2.5	10.1	0.5
DK-AR-11-31	0.41	0.00892	0.00205	0.00158	0.00007	0.19	9.0	2.1	10.2	0.4
DK-AR-11-32[a]	0.22	0.03552	0.00765	0.00165	0.00012	0.34	35.4	7.6	10.6	0.8
DK-AR-11-33[a]	0.32	0.00991	0.00436	0.00205	0.00011	0.12	10.0	4.4	13.2	0.7
DK-AR-11-34	0.42	0.01003	0.00242	0.00154	0.00006	0.17	10.1	2.4	9.9	0.4
DK-AR-11-35	0.27	0.01091	0.00372	0.00154	0.00008	0.15	11.0	3.8	9.9	0.5
DK-AR-11-36	0.27	0.01109	0.00361	0.00165	0.00008	0.15	11.2	3.6	10.7	0.5
DK-AR-11-37	0.33	0.01134	0.00291	0.00158	0.00007	0.17	11.4	2.9	10.2	0.5
DK-AR-11-38	0.29	0.00880	0.00359	0.00154	0.00008	0.13	8.9	3.6	9.9	0.5
DK-AR-11-39	0.26	0.01160	0.00314	0.00159	0.00007	0.17	11.7	3.2	10.2	0.5
DK-AR-11-40	0.32	0.01007	0.00297	0.00162	0.00007	0.16	10.2	3.0	10.5	0.5

(Continued)

Table 3. (*Continued*)

Spot	Th/U	^{207}Pb/^{235}U	Error (±2σ)	^{206}Pb/^{238}U	Error (±2σ)	ρ	^{235}U–^{207}Pb (Ma)	Error (±2σ)	^{238}U–^{206}Pb (Ma)	Error (±2σ)
DK-AR-21 (Dacite)										
DK-AR-21-01	0.20	0.01071	0.00122	0.00170	0.00004	0.22	10.8	1.2	10.9	0.3
DK-AR-21-02[a]	0.38	0.05204	0.00387	0.00215	0.00006	0.38	51.5	3.8	13.8	0.4
DK-AR-21-03	0.28	0.01529	0.00217	0.00174	0.00006	0.25	15.4	2.2	11.2	0.4
DK-AR-21-04	0.41	0.01518	0.00227	0.00171	0.00006	0.25	15.3	2.3	11.0	0.4
DK-AR-21-05[a]	0.14	0.03409	0.00381	0.00192	0.00007	0.33	34.0	3.8	12.4	0.5
DK-AR-21-06	0.26	0.01340	0.00236	0.00175	0.00007	0.23	13.5	2.4	11.3	0.5
DK-AR-21-07	0.24	0.01076	0.00220	0.00180	0.00008	0.20	10.9	2.2	11.6	0.5
DK-AR-21-08	0.29	0.01171	0.00271	0.00186	0.00009	0.21	11.8	2.7	12.0	0.6
DK-AR-21-09	0.25	0.01029	0.00187	0.00169	0.00006	0.20	10.4	1.9	10.9	0.4
DK-AR-21-10	0.14	0.01489	0.00224	0.00170	0.00006	0.24	15.0	2.3	10.9	0.4
DK-AR-21-11	0.26	0.01037	0.00194	0.00168	0.00006	0.20	10.5	2.0	10.8	0.4
DK-AR-21-12	0.32	0.01304	0.00235	0.00167	0.00007	0.22	13.2	2.4	10.8	0.4
DK-AR-21-13	0.26	0.01341	0.00271	0.00175	0.00008	0.22	13.5	2.7	11.2	0.5
DK-AR-21-14	0.24	0.00983	0.00220	0.00172	0.00007	0.19	9.9	2.2	11.1	0.5
DK-AR-21-15[a]	0.22	0.01518	0.00262	0.00626	0.00014	0.13	15.3	2.6	40.2	0.9
DK-AR-21-16	0.26	0.01478	0.00280	0.00180	0.00008	0.23	14.9	2.8	11.6	0.5
DK-AR-21-17	0.36	0.01183	0.00211	0.00183	0.00007	0.20	11.9	2.1	11.8	0.4
DK-AR-21-18	0.24	0.01088	0.00232	0.00177	0.00007	0.19	11.0	2.3	11.4	0.5
DK-AR-21-19[a]	0.28	0.02231	0.00418	0.00181	0.00009	0.27	22.4	4.2	11.7	0.6
DK-AR-21-20	0.31	0.01222	0.00282	0.00172	0.00008	0.20	12.3	2.8	11.1	0.5
DK-AR-21-21[a]	0.31	0.03022	0.00436	0.00192	0.00008	0.30	30.2	4.4	12.4	0.5
DK-AR-21-22	0.29	0.01036	0.00257	0.00179	0.00008	0.18	10.5	2.6	11.6	0.5
DK-AR-21-23	0.26	0.01175	0.00282	0.00172	0.00008	0.20	11.9	2.9	11.1	0.5
DK-AR-21-24	0.44	0.01311	0.00262	0.00172	0.00007	0.21	13.2	2.6	11.1	0.5
DK-AR-21-25	0.25	0.01334	0.00277	0.00177	0.00008	0.22	13.5	2.8	11.4	0.5
DK-AR-21-26	0.28	0.01231	0.00282	0.00180	0.00009	0.21	12.4	2.8	11.6	0.6
DK-AR-21-27	0.30	0.01585	0.00278	0.00186	0.00008	0.24	16.0	2.8	12.0	0.5
DK-AR-21-28	0.31	0.01134	0.00224	0.00176	0.00007	0.21	11.4	2.3	11.3	0.5
DK-AR-21-29[a]	0.18	0.02245	0.00268	0.00186	0.00006	0.28	22.5	2.7	12.0	0.4
DK-AR-21-30	0.21	0.01204	0.00176	0.00170	0.00006	0.22	12.1	1.8	11.0	0.4
DK-AR-21-31[a]	0.31	0.02599	0.00370	0.00192	0.00008	0.29	26.1	3.7	12.4	0.5
DK-AR-21-32	0.25	0.01542	0.00293	0.00182	0.00008	0.24	15.5	3.0	11.8	0.5
DK-AR-21-33	0.24	0.01158	0.00262	0.00183	0.00009	0.22	11.7	2.6	11.8	0.6
DK-AR-21-34	0.30	0.01156	0.00259	0.00168	0.00009	0.23	11.7	2.6	10.8	0.6
DK-AR-21-35[a]	0.19	0.02133	0.00298	0.00183	0.00008	0.30	21.4	3.0	11.8	0.5
DK-AR-21-36	0.17	0.01430	0.00248	0.00173	0.00008	0.25	14.4	2.5	11.1	0.5
DK-AR-21-37	0.33	0.01317	0.00274	0.00184	0.00009	0.23	13.3	2.8	11.9	0.6
DK-AR-21-38	0.33	0.01008	0.00163	0.00165	0.00006	0.23	10.2	1.7	10.7	0.4
DK-AR-21-39[a]	0.37	0.02504	0.00335	0.00186	0.00008	0.31	25.1	3.4	12.0	0.5
DK-AR-21-40	0.51	0.01364	0.00144	0.00166	0.00005	0.29	13.8	1.4	10.7	0.3

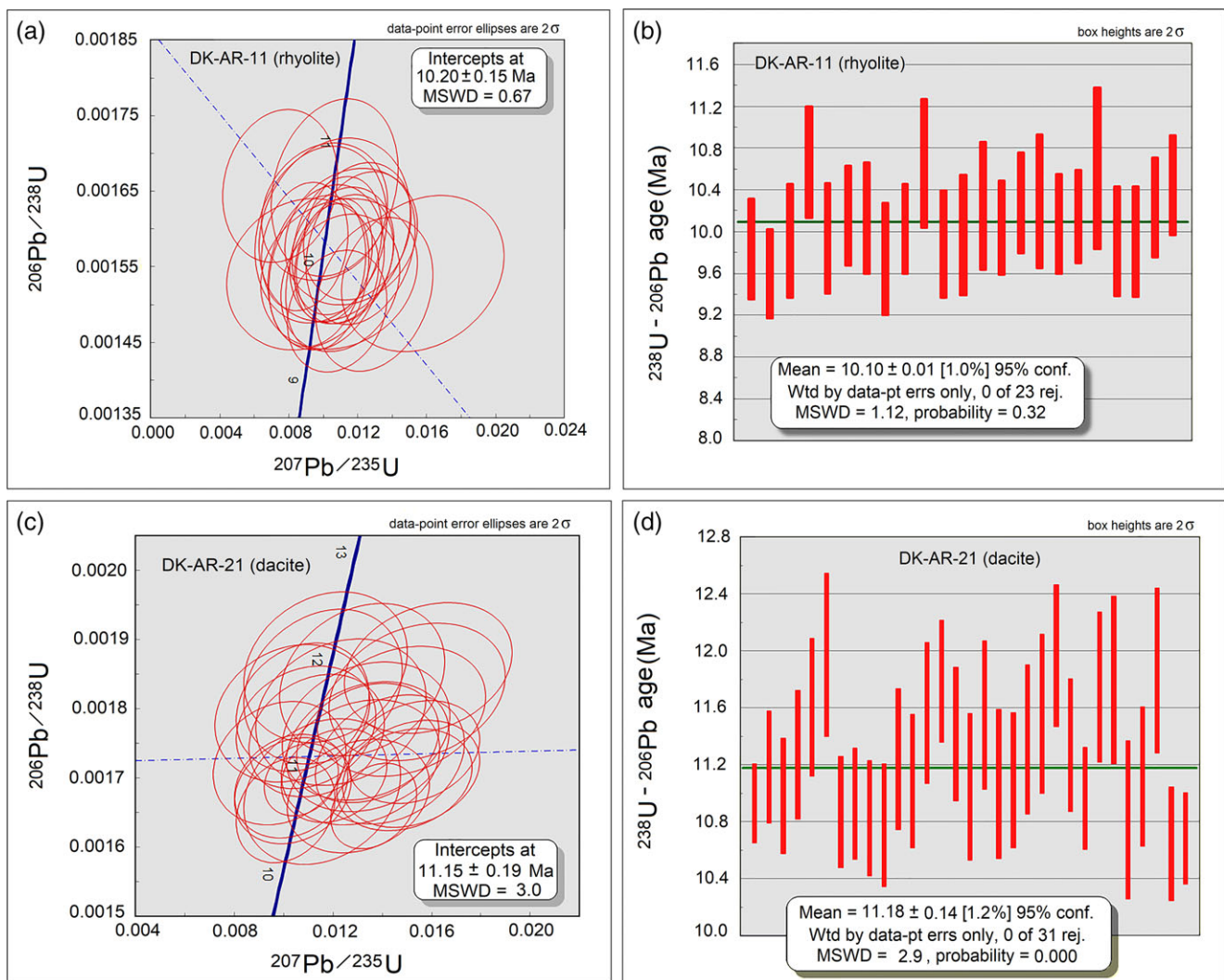[a]Excluded from Concordia diagram because of the high error.

Fig. 7. (Colour online) Zircon U–Pb concordia diagrams weighted mean ages and 2σ errors for samples (a, b) DKAR11 and (c, d) DKAR21.

4.b. Zircon preparation and U–Pb analytical techniques

Two samples (rhyolite DKAR11 and dacite DKAR21) were selected from the host rocks of Sari Gunay gold deposit for U–Pb LA-ICP-MS dating. Zircons separation for U–Pb LA-ICP-MS dating was performed at the Department of Geology in Bu-Ali Sina University Hamedan (Iran) using conventional mineral separation techniques, and were mounted on epoxy resin and polished. The polished zircon grains were studied by cathodoluminescence (CL) using a scanning electron microscope (Hitachi S- 3400N) and back-scatter imaging at Nagoya University (Japan). A total of 40 spots from 32 zircons of the sample DKAR11 (rhyolite) and 40 spots from 31 zircons of the sample DKAR21 (dacite) were analysed by LA-ICP-MS (Agilent 7700×) connected to laser ablation (NWR213 Electro Scientific Industries) at Nagoya University, Japan. ISOPLOT version 4.15 software (Ludwig, 2012) was used for U–Pb data evaluation. International reference zircons 91500 of age 1057 ± 14 Ma (Wiedenbeck *et al.* 2004) and OD-3 of age 32.8 ± 1.6 Ma (Iwano *et al.* 2013) were used as standard samples during analyses.

5. Results

5.a. Zircon U–Pb analyses

Cathodoluminescence (CL) (Fig. 6a, b) and microscopic images (Fig. 5h) show that the zircon grains have short to medium prismatic euhedral to subhedral shape and magmatic oscillatory textures.

5.a.1. Sample DKAR11 (rhyolite)

The Th/U ratios in the zircon grains from sample DKAR11 vary between 0.22 and 0.63 (Table 3), consistent with a magmatic origin. The spot analyses yielded a cluster concordia age of 10.20 ± 0.15 Ma (2σ error; mean squared weighted deviation, MSWD = 0.67) (Fig. 7a) with a weighted mean $^{206}Pb/^{238}U$ age of 10.10 ± 0.01 Ma (2σ error; MSWD = 1.12) (Fig. 7b). The cores and rims of the zoned zircon grains yield identical ages.

5.a.2. Sample DKAR21 (dacite)

LA-ICP-MS U–Pb zircon analyses from dacite sample DKAR21 are listed in Table 3. The data define a cluster concordia age of
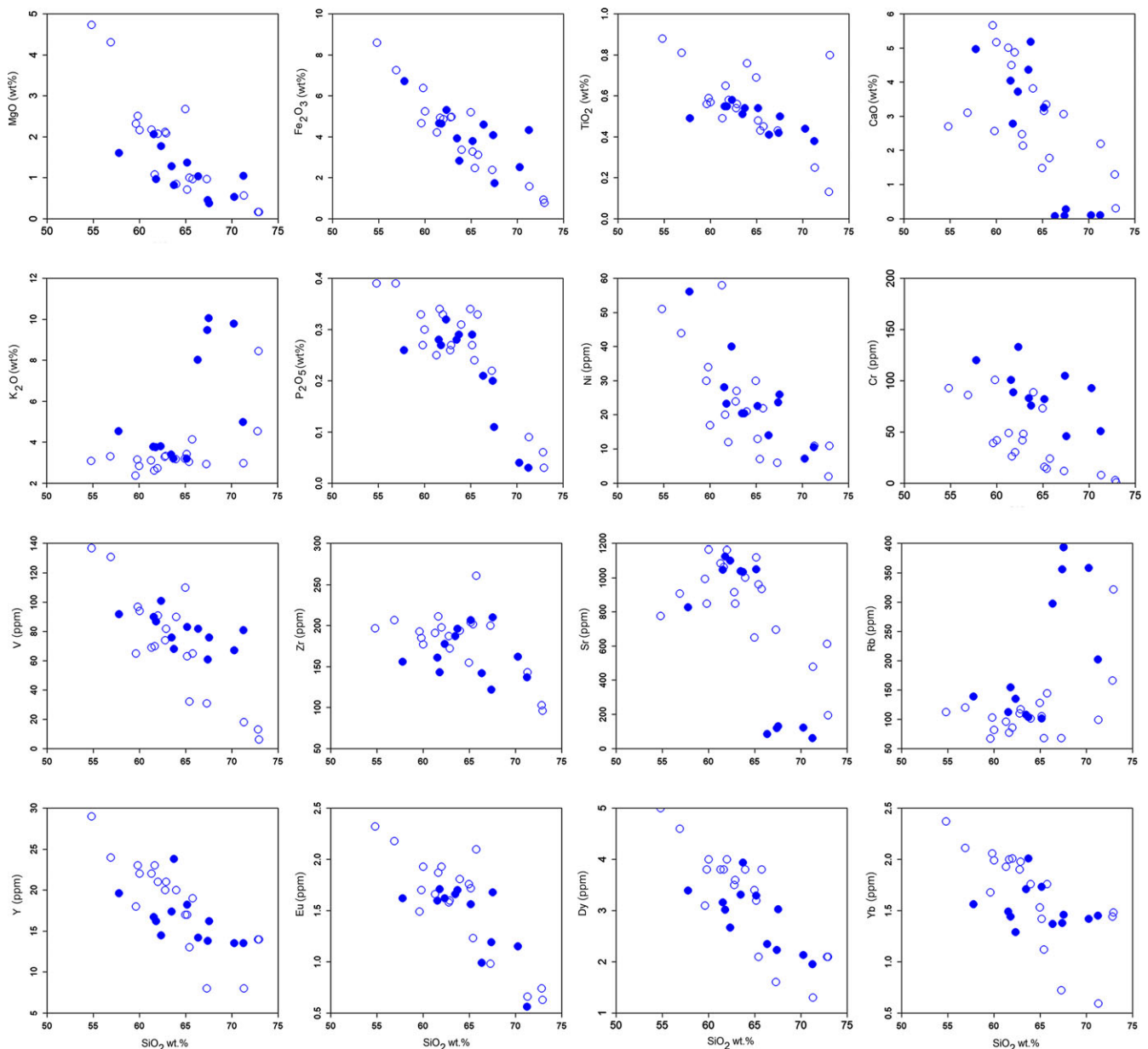
Fig. 8. (Colour online) Selected Harker variation diagrams for Sari Gunay adakitic rocks. Open circles are Sari Gunay volcanic samples analysed by Richards *et al.* (2006); closed circles are samples analysed in this study.

11.15 ± 0.19 Ma (2σ error; MSWD = 3.0) (Fig. 7c) and a weighted mean $^{206}Pb/^{238}U$ age of 11.18 ± 0.14 Ma (2σ error; MSWD = 2.9) (Fig. 7d) showing that these rocks were emplaced during middle–late Miocene time (Tortonian).

5.b. Whole-rock geochemistry

The geochemical data of the Sari Gunay volcanic rocks are listed in Table 2. The rocks are intermediate to felsic in composition with SiO_2 ranging from 57.78 to 71.21 wt%. Loss on ignition (LOI) values in the range 1.61–4.62 wt% indicate that the samples were affected by hydrothermal alteration or weathering. The Sari Gunay volcanic rocks are characterized by high ratios of Sr/Y (> 20; average 37.3) and La/Yb (> 20; average, 42.3); high SiO_2 (≥ 56 wt%; average, 64.9 wt%) and Sr (≥ 400 ppm; average, 645 ppm); low MgO (≤ 6 wt%; average, 1.11 wt%), Y (≤ 18 ppm;

average, 16.5 ppm) and Yb (≤ 1.9 ppm; average, 1.53 ppm); and weak negative Eu anomalies Eu*/ Eu (*c.* 0.81). As shown in Harker variation diagrams (Fig. 8), they display a decrease in Fe_2O_3, MgO, CaO, TiO_2, P_2O_5, Ni, Cr, V, Sr, Zr, Eu, Dy, Yb and Y as well as an increase in K_2O and Rb concentrations with increasing silica.

The Sari Gunay rocks shows enrichment in light rare earth elements (REEs) with respect to the heavy REEs, a flat heavy REEs pattern and a weak negative Eu anomaly Eu*/Eu (*c.* 0.81) (Fig. 9a). REE patterns of all samples are strongly fractionated (La_N/Yb_N *c.* 28). Moreover, a downward concavity of the middle REEs is shown by the pattern (Fig. 9a). In the primitive mantle-normalized multi-element diagram (Fig. 9b), the rocks display relative depletion of high-field-strength elements (HFSE) (i.e. Ti, Nb, Ta, Y, Zr, P).

In the AFM ($Na_2O + K_2O$; $FeO + Fe_2O_3$; MgO) triangular diagram (Fig. 10a), the Sari Gunay adakitic volcanic rocks show a calc-
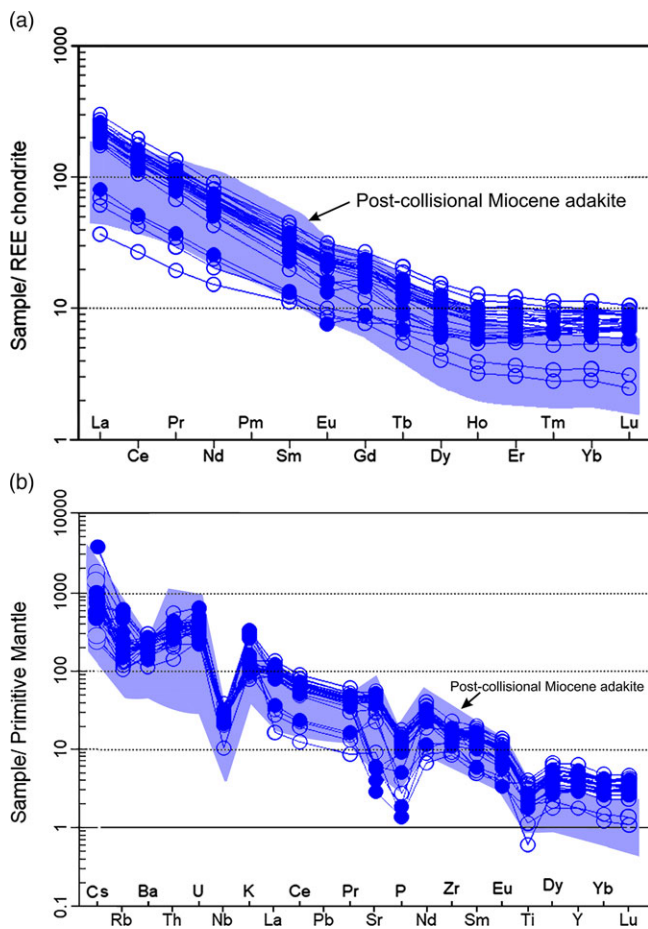
(a)

(b)

Fig. 9. (Colour online) (a) Chondrite-normalized REE and (b) primitive-mantle-normalized trace-element patterns for Sari Gunay adakitic rocks and their comparison with post-collisional Miocene ore-bearing adakites (Li *et al.* 2011). Normalized values for REE are from Boynton (1984) and normalizing values of the trace elements are from Sun & McDonough (1989). Open circles are Sari Gunay volcanic samples analysed by Richards *et al.* (2006).

alkaline nature. In the Th versus Co diagram after Hastie *et al.* (2007), the samples show high-K calc-alkaline nature and plot in the andesite dacite and rhyolite fields (Fig. 10b).

The Sari Gunay adakitic volcanic rocks contain normative orthoclase, quartz, albite, anorthite, hematite, biotite and rare ilmenite and calcite (Table 4). In the R1 (4Si − 11(Na+K) − 2(Fe+Ti)) − R2 (6Ca+2Mg+Al) diagram (De La Roche *et al.* 1980), the Sari Gunay volcanic rocks plot in the latite, quartz latite, dacite and rhyolite fields (Fig. 10c). Based on the Nb/Y versus Zr/TiO_2 diagram (Winchester & Floyd 1977), all except one sample from Sari Gunay plot in the trachyandesite field (Fig. 10d).

6. Discussion

6.a. Tectonic discrimination

The Sari Gunay volcanic rocks show some clear similarities to adakites (e.g. high Sr/Y and La/Yb ratios) when plotted on diagrams used for adakitic rocks. Based on the $(La)_N/(Yb)_N$ versus $(Yb)_N$ diagram of Martin (1986) and the La/Yb versus Yb diagram of Castillo *et al.* (1999), the rocks plot in the adakite field (Fig. 11a, b). In the Th/Yb versus Th/Sm diagram (Zhu *et al.* 2009), the Sari Gunay volcanic rocks plot in the field of post-collisional adakites (Fig. 11c). In

the Ta versus Yb tectonic discrimination diagram (Pearce *et al.* 1984), the samples plot in the volcanic arc (VA) and syn-collision (syn-COL) granitoid fields (Fig. 11d). Chondrite-normalized REEs and primitive-mantle-normalized trace-element patterns of the Sari Gunay rocks are comparable with patterns of post-collisional Miocene ore-bearing adakites in Tibet which are associated with ore-deposits (Li *et al.* 2011) (Fig. 9a, b).

6.b. Petrogenesis and geodynamic setting

Based on major- and trace-element characteristics, adakites can be classified into four groups with respect to their sources: (1) those derived from melting of a young and hot subducted oceanic slab consisting of metamorphosed basalt (amphibolite or eclogite) (Defant & Drummond, 1990; Castillo *et al.* 1999; Martin, 1999; Castillo, 2012; Rossetti *et al.* 2014; Omrani, 2018); (2) those derived by melting of a delaminated or thickened lower mafic crust in the stability field of clinopyroxene, amphibole, ± garnet and in a post-collision setting (Wang *et al.* 2006; Liu *et al.* 2008; Chiaradia, 2009; Karsli *et al.* 2010; Li *et al.* 2017); (3) those derived from melting of the metasomatized mantle wedge (Castillo *et al.* 1999; MacPherson *et al.* 2006; Richards & Kerrich 2007; Chiaradia, 2009; Azizi *et al.* 2019*a*); and (4) those derived by magma mixing (Guo *et al.* 2007; Qin *et al.* 2010).

Considering the La_N/Yb_N versus Yb_N diagram (Fig. 12a) and the Cr (ppm), P_2O_5 (wt%) and Th/Ce versus SiO_2 (wt%) diagrams (Fig. 12b, c, d) (Wang *et al.* 2006), the Sari Gunay samples plot close to the field defined by delaminated lower-crust-derived adakitic rocks (e.g. relatively low Yb contents, high La/Yb ratios and high Cr). Further, the Sari Gunay rocks have relatively negative Ti–Nb anomalies and low Ta contents similar to adakites (Fig. 9b; Table 2). The negative Ti–Nb anomalies and low Ti–Nb–Ta contents in adakites are related to equilibration of melts with residual hornblende and/or Fe–Ti oxides such as rutile, titanite and ilmenite (Rapp *et al.* 1991; Wolf & Wyllie, 1994; Rapp & Watson, 1995). Negative Eu anomalies may indicate a plagioclase free source (Hou *et al.* 2004). A flat heavy REE pattern associated with low heavy REE concentrations and high light over heavy REEs ratios ($La_N/Yb_N > 10$) indicates that the garnet was a stable residual phase during melting (Rapp *et al.* 1991; Wolf & Wyllie, 1994; Rapp & Watson, 1995). Medium REE patterns with weak concavities imply the presence of residual amphibole in the source (Gromet & Silver, 1987).

Samples from Sari Gunay are further characterized by MgO (0.37–2.06 wt%), TiO_2 (0.38–0.55 wt%), $CaO+Na_2O$ (0.28–9.36 wt%), Sr (*c.* 645 ppm) and K/Rb (< 280). High-SiO_2 adakites (HSA) compared to low-SiO_2 adakites (LSA) have lower MgO (0.5–4 wt%), lower TiO_2 (< 0.9 wt%), $CaO+Na_2O$ (< 11 wt%), Sr (< 1100 ppm), Cr/Ni (0.5–4.5) and K/Rb (< 1000). The Cr/Ni ratio in HSA ranges from 0.5 to 4.5 while in LSA this ratio ranges from 1 to 2.5. Pyroxene phenocrysts are absent from the HSA while they may be present in LSA (Martin *et al.* 2005). In the MgO versus SiO_2 and Cr/Ni versus TiO_2 diagrams (Martin *et al.* 2005), almost all Sari Gunay samples plot within the HSA field (Figs 13a, b). The Sari Gunay samples have Cr/Ni ratios between 2.1 and 5 and no pyroxene phenocrysts. Experimental results show that HSA can be generated by melting of basaltic materials such as eclogite or garnet amphibolite. The trace-element contents of these melts are similar to melts in equilibrium with a garnet-bearing residue (Rapp *et al.* 1991; Wolf & Wyllie, 1994; Rapp & Watson, 1995). In turn, LSA have been obtained by partial melting of a mantle peridotite (Sajona *et al.* 1996; Stern & Kilian,
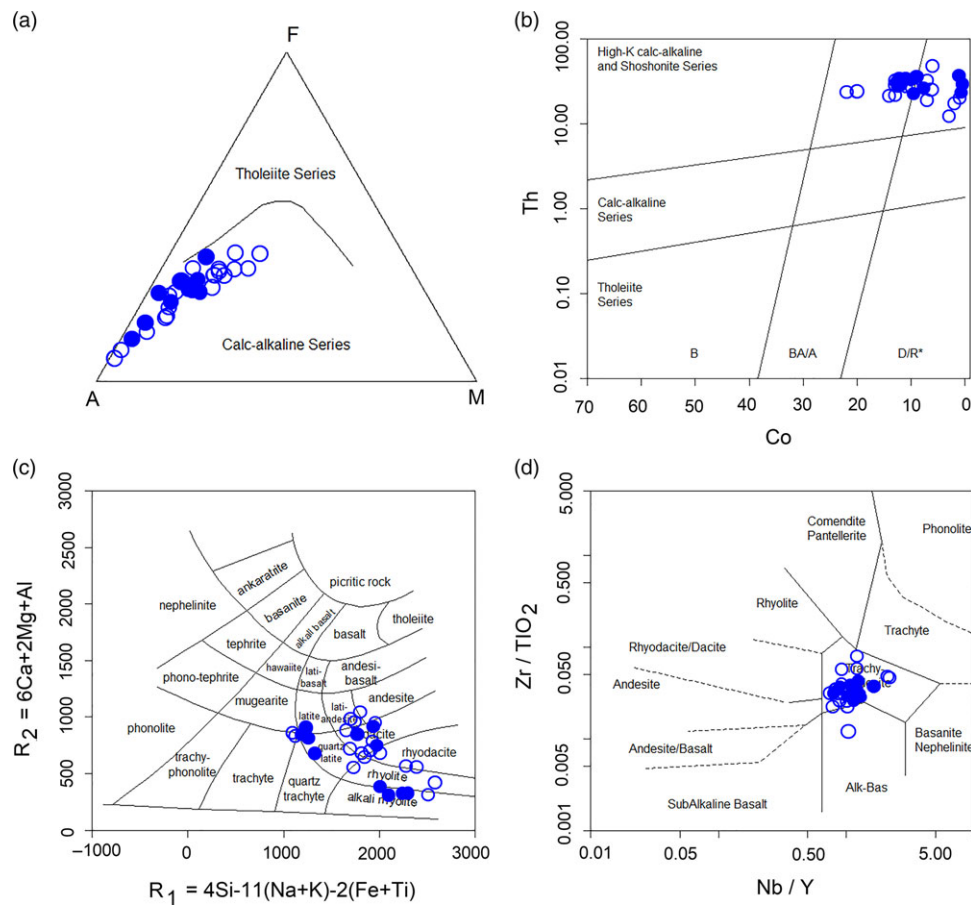
Fig. 10. (Colour online) (a) AFM diagram: A ($Na_2O + K_2O$), F ($FeO + Fe_2O_3$), M (MgO) (Irvine & Baragar, 1971); (b) Th versus Co diagram after Hastie *et al.* (2007); (c) R1–R2 diagram after De la Roche *et al.* (1980) for classification of the Sari Gunay adakitic rocks; and (d) Zr/TiO_2 versus Nb/Y diagram (after Winchester & Floyd, 1977). Open circles are Sari Gunay volcanic samples analysed by Richards *et al.* (2006). B – basalt; BA/A – basaltic andesite and andesite; D/R* – dacite and rhyolite (* indicates that latites and trachytes also fall in the D/R fields).

1996; Martin *et al.* 2005). Most Sari Gunay samples plot within the field of liquids obtained by experimental melting of basalts or amphibolites (Fig. 13a). The MgO content of the Sari Gunay samples is generally higher than that defined by the HSA field (Fig. 13a). It is argued that slightly higher MgO, Ni and Cr contents of the HSA (compared with experimental melts) is due to the interaction of the melt with mantle peridotite (Stern & Kilian, 1996; Rapp *et al.* 1999; Smithies, 2000; Prouteau *et al.* 2001).

Garnet and amphibole are essential residual phases during the generation of HSA. The negative correlation between Dy/Yb ratios and silica indicates that residual amphibole played a more important role than garnet in generating HSA melts (Davidson *et al.* 2013). Amphibole has important control on the medium REE contents during partial melting or during magma fractionation. Amphibole decreases the Dy/Yb ratio by increasing SiO_2, whereas garnet increases this ratio. The Sari Gunay samples display a strong negative correlation between Dy/Yb and silica (Fig. 13c). This indicates that amphibole was a major residual phase during melting. Based on experimental results (Kay *et al.* 1999), amphibole breaks down at depths of 40–50 km. Furthermore, ratios of different REEs such as La/Yb, La/Sm and Sm/Yb supply important information about the generation of adakitic melts residual mineralogy and relative crustal thicknesses. The La/Yb versus La diagram (Gao *et al.* 2007) suggests that partial melting was more important than fractional crystallization during the generation of the Sari Gunay rocks (Fig. 13d). The geochemical variation (Fig. 8) can be ascribed to

fractionation of plagioclase, biotite, titanite, apatite, Fe oxides and zircon during crystallization. Sr and Y are compatible in plagioclase and titanite. Consequently, their concentration has been decreased by fractionation of these mineral phases in the Sari Gunay adakitic rocks.

Low ratios of La/Yb (< 20), La/Sm (< 4) and Sm/Yb (< 3) generally indicate residual clinopyroxene, whereas higher ratios of such elements indicate that heavy REEs (such as Yb) were kept by garnet and amphibole in the residue (Kay *et al.* 1991; Haschke *et al.* 2002; Haschke & Günther, 2003; Karsli *et al.* 2019). The Sari Gunay rocks contain high ratios of La/Yb (*c.* 42.3) and La_N/Yb_N (*c.* 28.5), and moderately high La/Sm (*c.* 11.1) and Sm/Yb (*c.* 3.8) ratios. Schiano *et al.* (1995) reported that adakitic glassy inclusions in olivine crystals from ultramafic mantle xenoliths with very high La_N/Yb_N ratios (*c.* 48) could be evidence for interaction between slab melts and mantle peridotite. Similar signatures of the Sari Gunay adakitic rocks may reflect the interaction between lower-crustal garnet amphibolite and mantle peridotite. Based on the La_N/Yb_N versus Yb_N diagram (Martin, 1986), the Sari Gunay volcanic rocks were generated by partial melting of a garnet-amphibolite and metasomatized mantle peridotite source (Fig. 14).

The role of the metasomatized lithospheric mantle in the genesis of adakites in the northeastern SaSZ was emphasized by isotope data (see Azizi *et al.* 2014a). Late Miocene formation of the Sari Gunay composite volcano occurred contemporaneously

Table 4. CIPW normative mineralogy of the Sari Gunay gold deposit volcanic host rocks, Sanandaj–Sirjan zone, NW Iran. All DK-, K- and IR- Sari Gunay volcanic samples were analysed by Richards *et al.* (2006).

| Sample	DKAR02	DKAR04	DKAR06	DKAR07	DKAR08	DKAR11	DKAR21	DKAR23	DKAR25	EN6b	EN8	TSM7	DK03	DK05	DK06	DK18
Quartz	13.1	49.9	30.0	33.6	31.4	27.4	11.4	10.1	10.6	18.6	17.5	22.0	31.6	10.7	12.6	21.8
Orthoclase	20.0	27.1	54.9	45.0	56.6	58.7	18.4	17.6	23.1	17.0	17.1	15.8	12.7	9.7	7.3	14.6
Albite	42.3	3.0	1.6	3.0	1.9	1.9	44.3	45.0	32.7	35.1	37.1	36.0	27.5	40.8	37.4	34.7
Anorthite	12.1	0.3	0.0	0.0	0.2	0.7	10.9	9.7	11.0	16.6	15.1	14.2	5.1	12.6	10.9	10.6
Wollastonite	0.0	0.0	0.0	0.0	0.0	0.0	2.3	3.6	5.0	3.0	2.0	0.0	0.0	0.1	0.0	0.0
Ilmenite	0.4	0.0	0.0	0.0	0.0	0.0	0.3	0.4	0.5	0.2	0.2	0.1	0.3	0.4	0.5	0.5
Hematite	4.6	4.3	4.1	4.6	2.5	1.7	5.3	4.7	6.7	2.8	3.9	3.8	5.2	7.3	8.6	5.0
Apatite	0.6	0.1	0.2	0.1	0.1	0.3	0.8	0.7	0.6	0.7	0.7	0.7	0.8	0.9	0.9	0.6
Biotite	3.2	3.5	1.5	3.4	1.8	1.2	5.8	6.8	5.3	2.7	4.2	4.5	8.9	14.2	15.6	7.0
Calcite	0.2	6.0	3.9	4.2	3.6	5.9	0.0	0.0	0.0	0.0	0.0	1.2	3.4	0.0	1.4	1.7
Sum	96.5	94.2	96.2	94.0	98.1	97.7	99.6	98.5	95.6	96.7	97.7	98.3	95.5	96.7	95.2	96.3
Sample	**DK19**	**DK20**	**DK40**	**DK41**	**DK44**	**DK45**	**K60**	**K61**	**K62**	**K63**	**K64**	**DK65**	**K66**	**IR57**	**IR59**	
Quartz	22.9	23.8	20.2	20.9	33.5	19.6	16.5	34.5	15.4	20.8	29.0	15.8	16.3	22.3	17.4	
Orthoclase	14.9	12.8	16.9	22.2	26.5	11.4	13.4	49.5	13.0	18.6	16.3	11.9	8.7	15.1	15.7	
Albite	34.0	27.9	35.4	37.9	28.2	33.4	35.8	8.0	40.5	36.6	38.6	35.4	35.5	41.0	44.8	
Anorthite	8.9	11.0	16.9	6.7	6.0	19.3	15.1	1.3	18.6	13.9	10.3	17.9	19.2	12.1	10.7	
wollastonite	0.0	0.0	0.0	0.0	0.0	1.2	3.4	0.0	0.6	0.0	0.0	2.4	2.8	0.7	1.8	
Ilmenite	0.5	0.5	0.1	0.1	0.0	0.2	0.2	0.0	0.2	0.0	0.0	0.2	0.2	0.1	0.1	
Hematite	5.0	6.4	3.4	3.1	0.9	4.9	4.2	0.8	4.9	3.3	1.6	5.2	4.7	2.4	2.5	
Apatite	0.6	0.6	0.7	0.8	0.1	0.8	0.6	0.1	0.8	0.6	0.2	0.7	0.8	0.5	0.6	
Biotite	6.9	8.3	2.8	3.2	0.5	6.8	7.2	0.5	3.6	2.3	1.8	7.1	7.7	3.2	3.3	
Calcite	2.4	2.8	0.5	1.7	1.5	0.0	0.0	2.7	0.0	0.9	0.8	0.0	0.0	0.0	0.0	
Sum	96.1	94.1	96.8	96.7	97.2	97.5	96.3	97.5	97.6	97.2	98.6	96.7	95.8	97.4	96.9	
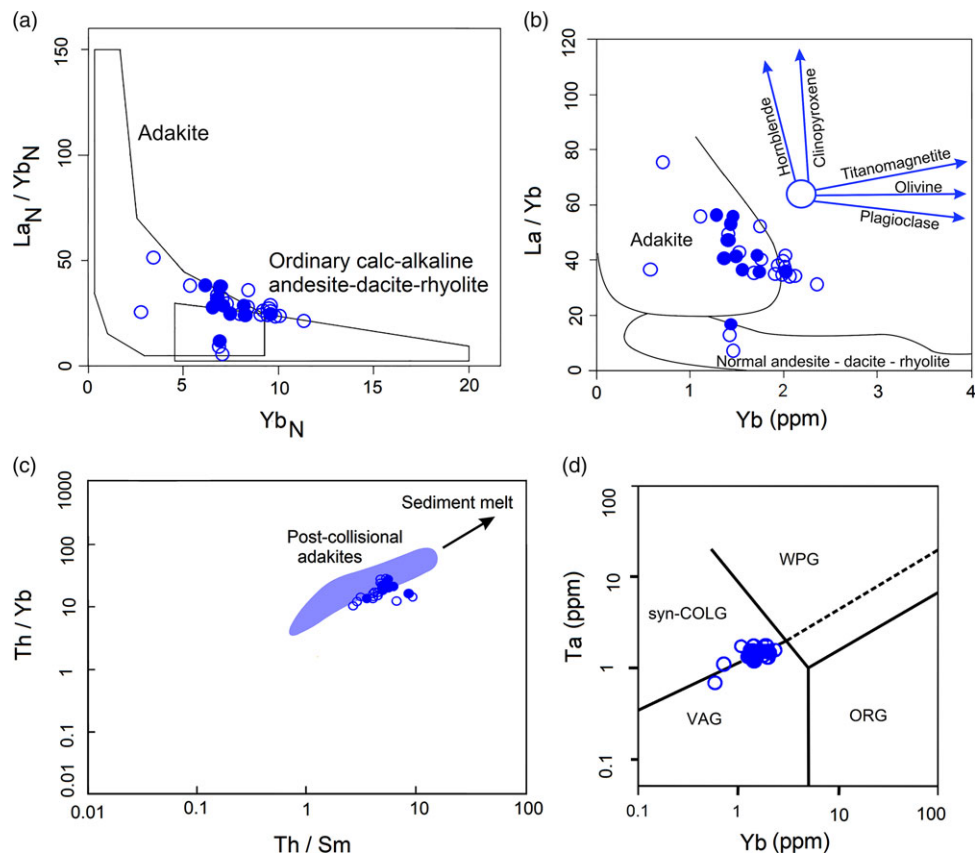
Fig. 11. (Colour online) Tectonic discrimination diagrams for Sari Gunay adakitic rocks. (a) (La)$_N$/(Yb)$_N$ versus (Yb)$_N$ diagram after Martin (1986); (b) La/Yb versus Yb diagram after Castillo *et al.* (1999); (c) Th/Yb versus Th/Sm diagram (Zhu *et al.* 2009); and (d) Ta versus Yb tectonic discrimination diagram (Pearce *et al.* 1984). Open circles are Sari Gunay volcanic samples analysed by Richards *et al.* (2006). VAG – volcanic-arc granites; WPG – within-plate granites; ORG – ocean ridge granites; syn-COLG – syn-collision granites.
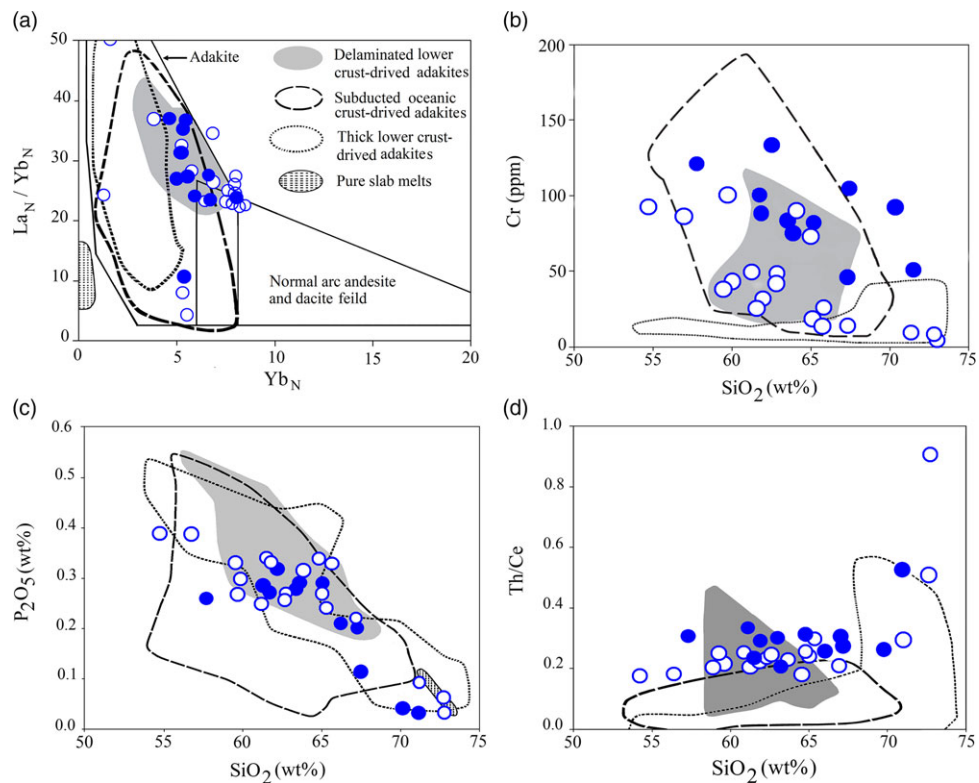
Fig. 12. (Colour online) Genetic classification diagrams for adakitic rocks: (a) La$_N$/Nb$_N$ versus Yb$_N$; (b) Cr (ppm) versus SiO$_2$; (c) P$_2$O$_5$ (wt%) versus SiO$_2$; and (d) Th/Ce versus SiO$_2$ (wt%) diagrams (Wang *et al.* 2006). Sari Gunay samples plot in the field of delaminated lower-crust-derived adakites. Open circles are Sari Gunay volcanic samples analysed by Richards *et al.* (2006).
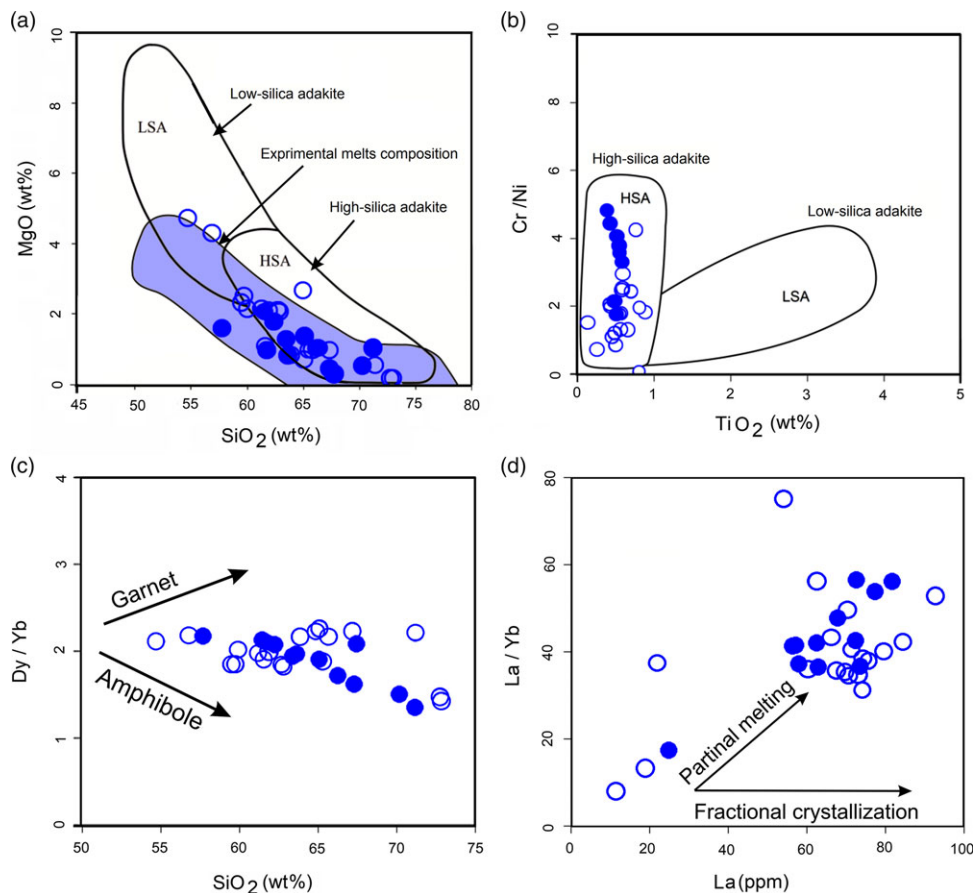
Fig. 13. (Colour online) (a, b) Diagrams for discriminating high-silica (HSA) and low-silica (LSA) adakite types: (a) MgO (wt%) versus SiO$_2$ (wt%) and (b) Cr/Ni versus TiO$_2$ (Martin *et al.* 2005). (c) Dy/Yb versus SiO$_2$ diagram showing that amphibole rather than garnet as a residual phase played an important role in the generation of the Sari Gunay adakitic rocks (Davidson *et al.* 2013). (d) La/Yb versus La (ppm) diagram (Gao *et al.* 2007) showing the role of partial melting during the generation of the Sari Gunay adakites. Open circles are Sari Gunay volcanic samples analysed by Richards *et al.* (2006); closed circles are samples analysed in this study.
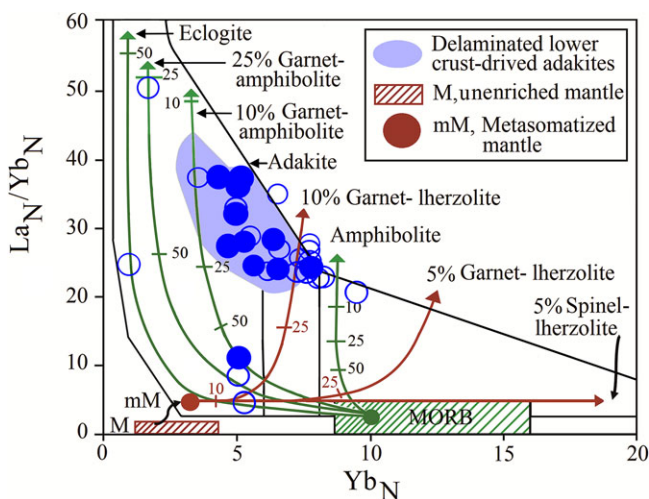
Fig. 14. (Colour online) La$_N$/Yb$_N$ versus Yb$_N$ diagram (Martin, 1986). Sari Gunay samples can be generated by partial melting of a 10% garnet-amphibolite source associated with 10% garnet-metasomatized mantle peridotite. The field of delaminated lower-crust-derived adakites is from Wang *et al.* (2006). Mid-ocean-ridge basalt (MORB) source and normalizing values of the trace elements from Sun & McDonough (1989). Open circles are Sari Gunay volcanic samples analysed by Richards *et al.* (2006).

with adakitic magmatism in the the Ghorveh–Bijar area, such as the Akhikamal volcanic dome with an age of 10.4 Ma (Azizi *et al.* 2014*a*). Based on the results of the study by Azizi *et al.* (2014*a*), the Sr–Nd isotope ratios indicate that late Miocene adakitic magmatic rocks in the Ghorveh–Bijar area were derived by partial melting of lower continental crust and a metasomatized lithospheric mantle. The Moho depths of 45–47 km in the Sari Gunay area (Dehghani & Makris, 1983) emphasize the likelihood of partial melting of the lower continental crust and the mantle lithosphere beneath it (Fig. 15). As described earlier in this section, previous experimental results (Kay *et al.* 1999) show that amphibole breaks down at depths of 40–50 km.

MASH (melting, assimilation, storage and homogenization) zones are thought to form beneath near the Moho due to density contrasts (Hildreth & Moorbath, 1988). In such zones, hybrid intermediate magmas with cumulate residues containing amphibole, olivine, pyroxene, plagioclase and garnet will form (De Bari & Coleman, 1989; Jagoutz *et al.* 2007; Richards, 2009). Amphibole-rich cumulates can act as a sponge storing up to 20% water in the original magma flux (Davidson *et al.* 2007). Magmas produced in lower crustal MASH zones can have high Sr/Y and La/Yb ratios due to preferential partitioning of Y, Yb, medium REEs and heavy REEs into residual amphibole and garnet (Green & Pearson, 1985;
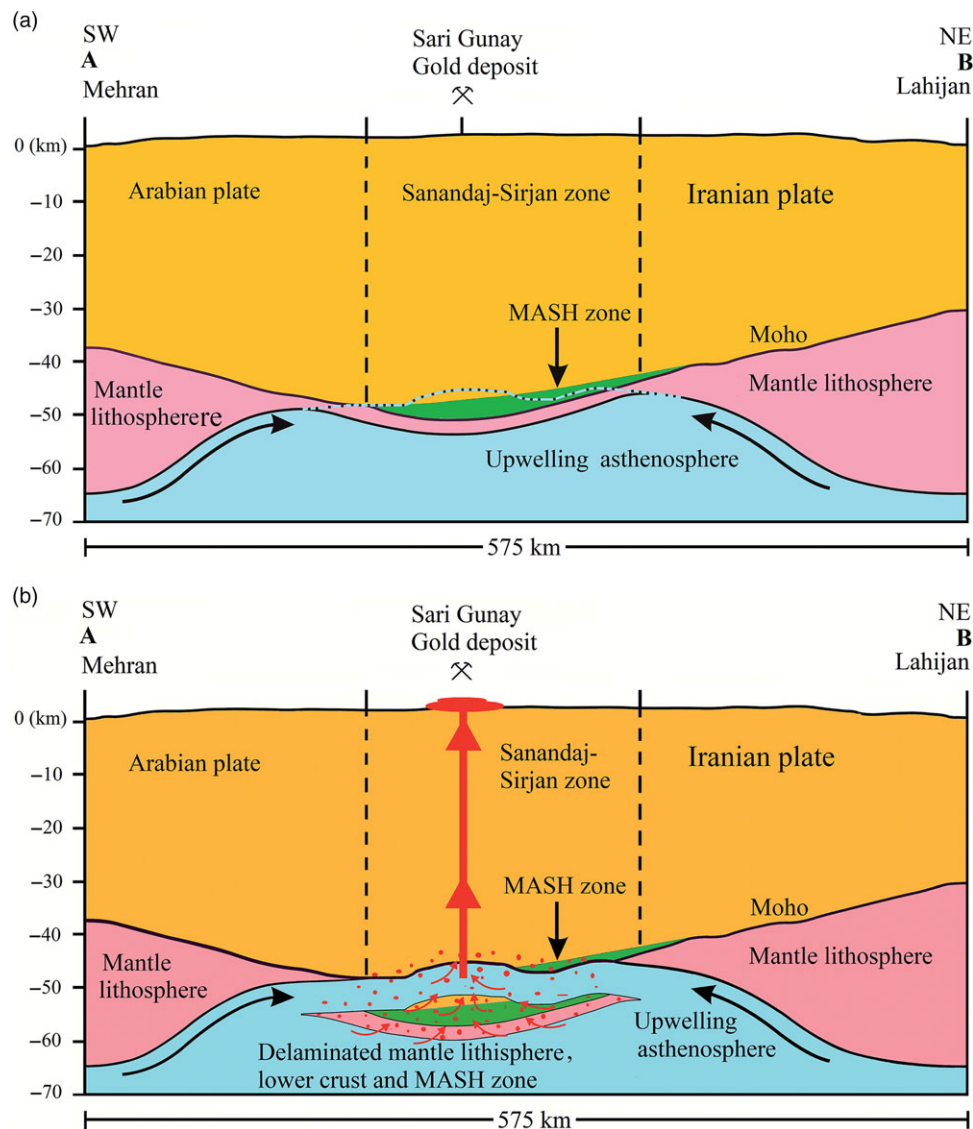
Fig. 15. (Colour online) Schematic geodynamic model for the generation of adakitic rocks of the Sari Gunay gold deposit. (a) The crustal thickness or Moho depth in NW Iran before delamination (Moho profile from Mehran to Lahijan, line A–B shown in Fig. 1); and (b) adakite formation by lithospheric delamination (delamination includes part of the lower crust and the metasomatized lithosphere mantle) and interaction with melts coming from the upwelling asthenospheric mantle. Crustal thickness (i.e. depth of Moho) is from Dehghani & Makris (1983).

Richards, 2009). It seems likely that MASH zones also played a role in generating the Sari Gunay adakitic host rock. Hornblende differentiation or residual hornblende, as well as partial melting of calc-alkaline mafic bodies in the lower crust, were proposed for the formation of Miocene adakites in the northeastern SaSZ (Azizi *et al.* 2011; Azizi *et al.* 2019a; Rabiee *et al.* 2020). However, a post-collision extension environment can be an alternative explanation for the occurrence of these rocks. The generation of mafic alkaline (shoshonitic or hawaiitic) magmas commonly occurs by upwelling of the subduction-metasomatized asthenosphere and attenuated lithosphere (Luhr, 1997; Paquette *et al.* 2003).

The concept of continental lithospheric mantle delamination, which was introduced by Bird (1978, 1979), includes the detachment and sinking of dense lithospheric mantle with or without portions of lower crust into the underlying asthenosphere. In addition, delamination is the result of thinned or absent mantle lithosphere under thickened crust. Rocks with adakitic geochemical features derived from the

delaminated lower crust were reported from the Alpine–Himalayan collisional belt such as the late Oligocene adakites in the southern Tibet (Chung *et al.* 2003) and Early Cretaceous adakitic lavas in the Songliao basin NE China (Ji *et al.* 2019). However, the evidence indicates that in our study area the melts with adakitic signatures were generated in a post-collision extension tectonic regime due to the upwelling and heating of hot asthenosphere associated with delamination of a thickened crust and lithosphere. It is suggested that melt formation within the delaminated segment, including lower crustal amphibolites and mantle lithosphere, followed by MASH zone processes led to the generation of the Sari Gunay adakitic volcanic host rocks (Fig. 15).

7. Conclusions

The Sari Gunay gold deposit is located within a composite volcanic complex consisting of massive to flow-banded lava flows, lahars and pyroclastic rocks. Based on whole-rock major- and

trace-element analyses, the lava flows of Sari Gunay deposit consist of latite, quartz latite, dacite and rhyolite. The rhyolites and latites belong to the shoshonite series, whereas dacites and quartz latites belong to the high-K calc-alkaline series. Almost all Sari Gunay volcanic rocks plot within the high-SiO_2 adakitic field. U–Pb zircon dating shows that the volcanic rocks formed at 11.18 ± 0.14 Ma and 10.10 ± 0.01 Ma. Their generation is related to asthenospheric upwelling, followed by the melting of delaminated crust consisting of amphibolite and mantle peridotite, as well as MASH zone processes in the lower crust.

References

Aghazadeh M, Castro A, Badrzadeh Z and Vogt K (2011) Post-collisional polyclinic plutonism from the Zagros hinterland: the Shaivar Dagh plutonic complex Alborz belt Iran. *Geological Magazine* **148**, 980–1008.

Alavi M (1994) Tectonic of the Zagros orogenic belt of Iran: new data and interpretation. *Tectonophysics* **229**, 211–38.

Alirezaei A, Arvin M and Dargahi S (2017) Adakite-like signature of porphyry granitoid stocks in the Meiduk and Parkam porphyry copper deposits NE of Shahr-e-Babak Kerman Iran: constrains on geochemistry. *Ore Geology Reviews* **88**, 370–83.

Alirezaei S and Hassanzadeh J (2012) Geochemistry and zircon geochronology of the Permian A-type Hasanrobat granite Sanandaj-Sirjan belt. A new record of the Gondwana breakup in Iran. *Lithos* **151**, 122–34.

Allen M, Jackson J and Walker R (2004) Late Cenozoic reorganization of the Arabia –Eurasia collision and the comparison of short–term and longterm deformation rates. *Tectonics* **23**, doi: 10.1029/2003TC001530.

Asadi HH, Kianpouryan S, Lu YJ and McCuaig TC (2014) Exploratory data analysis and C–A fractal model applied in mapping multi-element soil anomalies for drilling: A case study from the Sari Gunay epithermal gold deposit NW Iran. *Journal of Geochemical Exploration* **145**, 233–41.

Azizi H, Asahara Y, Mehrabi B and Chung SL (2011) Geochronological and geochemical constraints on the petrogenesis of high-K granite from the Suffiabad area Sanandaj-Sirjan Zone NW Iran. *Chemie der Erde-Geochemistry* **71**, 363–76.

Azizi H, Asahara Y, Motohiro T, Takemura K and Razyani S (2014a) The role of heterogenetic mantle in the genesis of adakites northeast of Sanandaj northwestern Iran: *Chemie der Erde* **74**, 87–97.

Azizi H, Asahara Y and Tsuboi M (2014b) Quaternary high-Nb basalt: existence of young oceanic crust under the sanadaj-Sirjan zone NW Iran: *International Geology Review* **56**, 167–86.

Azizi H, Hadad S, Stern RJ and Asahara Y (2019a) Age geochemistry and emplacement of the ˜ 40-Ma Baneh granite–appinite complex in a transpressional tectonic regime Zagros suture zone northwest Iran. *International Geology Review* **61**, 195–223.

Azizi H, Kazemi T and Asahara Y (2017) A-type granitoid in Hasansalaran complex northwestern Iran: Evidence for extensional tectonic regime in northern Gondwana in the Late Paleozoic. *Journal of Geodynamics* **108**, 56–72.

Azizi H and Moinevaziri H (2009) Review of the tectonic setting of Cretaceous to Quaternary volcanism in northwestern Iran. *Journal of Geodynamics* **47**, 167–79.

Azizi H, Stern RJ, Topuz G, Asahara Y and Shafaii Moghadam H (2019b) Late Paleocene adakitic granitoid from NW Iran and comparison with adakites in the NE Turkey: Adakitic melt generation in normal continental crust. *Lithos* **346–347**, 105151, https://doi.org/10.1016/j.lithos.2019.105151

Azizi H, Zanjefili-Beiranvand M and Asahara Y (2015) Zircon U–Pb ages and petrogenesis of a tonalite–trondhjemite–granodiorite (TTG) complex in the northern Sanandaj–Sirjan zone northwest Iran: Evidence for Late Jurassic arc–continent collision. *Lithos* **216**, 178–95.

Barber DE, Stockli DF, Horton BK and Koshnaw RI (2018) Cenozoic exhumation and foreland basin evolution of the Zagros orogen during the Arabia-Eurasia collision western Iran. *Tectonics* **37**, 4396–420.

Berberian F, Muir ID, Pankhurst RJ and Berberian M (1982) Late Cretaceous and Early Miocene Andean type plutonic activity in northern Makran and central Iran. *Journal of the Geological Society of London* **139**, 605–14.

Berberian M and King GCP (1981) Towards a paleogeography and tectonic evolution of Iran. *Canadian Journal of Earth Sciences* **18**, 210–65.

Bird P (1978) Initiation of intracontinental subduction in the Himalaya. *Journal of Geophysical Research* **83**, 4975–87.

Bird P (1979) Continental Delamination and the Colorado Plateau. *Journal of Geophysical Research* **84**, 7561–71.

Boccaletti M, Innoncenti F, Manetti P, Mazzuoli R, Motamed A, Paquare A, Radicati de Brozolo F and Amin Sobhani E (1976) Neogene and Quaternary volcanism of the Bijar area (western Iran). *Bulletin of Volcanology* **40–42**, 121–35.

Boynton WV (1984) Cosmochemistry of the rare earth elements: meteorite studies. In *Rare Earth Element Geochemistry* (ed. P Henderson), pp. 63–114. Amsterdam: Elsevier, *Developments in Geochemistry no. 2.*

Castillo PR (2012) Adakite petrogenesis. *Lithos* **134–135**, 304–16.

Castillo PR, Janney PE and Solidum RU (1999) Petrology and geochemistry of Camiguin island southern Philippines: insights to the source of adakites and other lavas in a complex arc setting. *Contributions to Mineralogy and Petrology* **134**, 33–51.

Chiaradia M (2009) Adakite-like magmas from fractional crystallization and melting-assimilation of mafic lower crust (Eocene Macuchi arc Western Cordillera Ecuador). *Chemical Geology* **265**, 468–87.

Chung SL, Liu DY, Ji JQ, Chu MF, Lee HY, Wen DJ, Lo CH, Lee TY, Qian Q and Zhang Q (2003) Adakites from continental collision zones: melting of thickened lower crust beneath southern Tibet. *Geology* **31**, 1021–24.

Davidson J, Turner S, Handley H, Macpherson C and Dosseto A (2007) Amphibole "sponge" in arc crust. *Geology* **35**, 787–90.

Davidson J, Turner S and Plank T (2013) Dy/Dy*: variations arising from mantle sources and petrogenetic processes. *Journal of Petrology* **54**, 525–37.

De Bari SM and Coleman RG (1989) Examination of the deep levels of an island arc: Evidence from the Tonsina ultramafic-mafic assemblage Tonsina Alaska. *Journal of Geophysical Research* **94**, 4373–439.

Defant MJ and Drummond MS (1990) Derivation of some modern arc magmas by melting of young subducted lithosphere. *Nature* **347**, 662–65.

Dehghani GA and Makris T (1983) The gravity field and crustal structure of Iran. Geodynamic project (Geotraverse) in Iran. Geological Survey of Iran, Final Report number **51**, 51–68.

De la Roche H, Leterrier J, Grandclaude P and Marchal M (1980) A classification of volcanic and plutonic rocks using R1-R2 diagrams and major-element analyses: its relation with current nomenclature. *Chemical Geology* **29**, 83–210.

Delavari M, Amini S, Schmitt AK, McKeegan KD and Harrison TM (2014) U–Pb geochronology and geochemistry of Bibi-Maryam pluton eastern Iran: Implication for the late stage of the tectonic evolution of the Sistan Ocean. *Lithos* **200**, 197–211.

Dewey JF, Pitman WC, Ryan WBF and Bonnin J (1973) Plate tectonics and the evolution of the Alpine System. *Geological Society of America Bulletin* **84**, 3137–80.

Gao YF, Hou ZQ, Kamber BS, Wei RH, Meng XJ and Zhao RS (2007) Adakite-like porphyries from the southern Tibetan continental collision zones: evidence for slab melt metasomatism. *Contributions to Mineralogy and Petrology* **153**, 105–20.

Ghasemi A and Talbot CJ (2005) A new tectonic scenario for the Sanandaj-Sirjan Zone (Iran). *Journal of Asian Earth Sciences* **26**, 683–93.

Ghorbani MR and Bezenjani RN (2011) Slab partial melts from the metasomatizing agent to adakite Tafresh Eocene volcanic rocks Iran. *Island Arc* **20**, 188–202.

Graniana H, Tabatabaei SH, Asadi HH and Carranza EJM (2014) Multivariate regression analysis of lithogeochemical data to model subsurface mineralization: a case study from the Sari Gunay epithermal gold deposit NW Iran. *Journal of Geochemical Exploration* **148**, 249–58.

Green TH and Pearson NJ (1985) Experimental determination of REE partition coefficients between amphibole and basaltic to andesitic liquids at high pressure. *Geochimica et Cosmochimica Acta* **49**, 1465–68.

Gromet LP and Silver L (1987) REE variations across the Peninsular Ranges Batholith: implications for batholithic petrogenesis and crustal growth in magmatic arcs. *Journal of Petrology* **28**, 75–125.

Guo ZF, Wilson M and Liu JQ (2007) Post-collisional adakites in south Tibet: products of partial melting of subduction-modified lower crust. *Lithos* **96**, 205–224.

Haschke M and Günther A (2003) Balancing crustal thickening in arc by tectonic vs. magmatic means. *Geology* **31**, 933–36.

Haschke M, Siebel W, Günther A and Scheuber E (2002) Repeated crustal thickening and recycling during the Andean orogeny in North Chile (21°–26°S). *Journal of Geophysical Research* **107**, 6–18.

Hassanzadeh J, Stockli DF, Horton BK, Axen GJ, Stockli LD and Grove M (2008) U-Pb zircon geochronology of late Neoproterozoic- Early Cambrian granitoids in Iran: Implications for paleogeography magmatism and exhumation history of Iranian basement. *Tectonophysics* **451**, 71–96.

Hassanzadeh J and Wernicke BP (2016) The Neotethyan Sanandaj-Sirjan Zone of Iran as an archetype for passive margin-arc transitions. *Tectonics* **35**, 586–621.

Hastie AR, Kerr AC, Pearce JA and Mitchell SF (2007) Classification of altered volcanic Island arc rocks using immobile trace elements: development of the th–co discrimination diagram. *Journal of Petrology* **48**, 2341–57.

Hildreth W and Moorbath S (1988) Crustal contributions to arc magmatism in the Andes of central Chile. *Contributions to Mineralogy and Petrology* **98**, 455–89.

Hou ZQ, Gao YF, Qu XM, Rui ZY and Mo XX (2004) Origin of adakitic intrusives generated during mid-Miocene east–west extension in southern Tibet. *Earth and Planetary Science Letters* **220**, 139–55.

Irvine TN and Baragar WRA (1971) A guide to the chemical classification of the common volcanic rocks. *Canadian Journal of Earth Sciences* **8**, 523.

Iwano H, Orihashi Y, Hirata T, Ogasawara M, Danhara T, Horie K, Hasebe N, Sueoka S, Tamura A, Hayasaka Y and Katsube A (2013) An inter-laboratory evaluation of OD-3 zircon for use as a secondary U–Pb dating standard. *Island Arc* **22**, 382–94.

Jagoutz O, Muntener O, Ulmer P, Pettke T, Burg JP, Dawood H and Hussain S (2007) Petrology and mineral chemistry of lower crustal intrusions: The Chilas Complex Kohistan (NW Pakistan). *Journal of Petrology* **48**, 1894–953.

Jahangiri A (2007) Post-collisional Miocene adakitic volcanism in NW Iran: geochemical and geodynamic implications. *Journal of Asian Earth Science* **30**, 433–47.

Jamali H, Dilek Y, Daliran F, Yaghubpur AM and Mehrabi B (2010) Metallogeny and tectonic evolution of the Cenozoic Ahar-Arasbaran volcanic belt northern Iran. *International Geology Review* **52**, 608–30.

Jamali H and Mehrabi B (2015) Relationships between arc maturity and Cu–Mo–Au porphyry and related epithermal mineralization at the Cenozoic Arasbaran magmatic belt. *Ore Geology Reviews* **65**, 481–501.

Jamshidi K, Ghasemi H, Laicheng M and Sadeghian M (2018) Adakite magmatism within the Sabzevar ophiolite zone NE Iran: U-Pb geochronology and Sr-Nd isotopic evidences. *Geopersia* **8**, 111–30.

Ji Zh, Meng Q, Wan Ch, Ge WCh, Yang H, Zhang YL, Dong Y and Jin X (2019) Early Cretaceous adakitic lavas and A-type rhyolites in the Songliao Basin NE China: implications for the mechanism of lithospheric extension. *Gondwana Research* **71**, 28–48.

Karsli O, Dokuz A, Kandemir R, Aydin F, Schmitt AK, Ersoy EY and Alyildiz C (2019) Adakite-like parental melt generation by partial fusion of juvenile lower crust Sakarya Zone NE Turkey: A far-field response to break-off of the southern Neotethyan oceanic lithosphere. *Lithos* **338–339**, 58–72.

Karsli O, Dokuz A, Uysal I, Aydin F, Kandemir R and Wijbrans RJ (2010) Generation of the Early Cenozoic adakitic volcanism by partial melting of mafic lower crust Eastern Turkey: implications for crustal thickening to delamination. *Lithos* **114**, 109–20.

Kay SM, Mpodozis C and Coira B (1999) Neogene magmatism tectonism and mineral deposits of the central Andes (22° to 33°S latitude). In *Geology and Ore Deposits of the Central Andes* (ed. BJ Skinner), 27–59. Littleton: Society of Economic Geologists, Special Publication no. **7**.

Kay SM, Mpodozis C, Ramos VA and Munizaga F (1991) Magma source variations for mid-late Tertiary magmatic rocks associated with a shallowing subduction zone and a thickening crust in the Central Andes (28–33°S). In *Andean– Magmatism and its Tectonic Setting* (eds RS Harmon and CW Rapela), pp. 113–37. Geological Society of America, Special Paper no. 265.

Khan Nazar NH, Jalali A, Saidi A, Helmi F, Mohtat T, Bahreh M, Zohrab E, Ghaemi J and Haddadan H (2015) *Geological map of Iran 1:100000 Series Sheet No. 5660 (Kohin)*. Tehran: Geological Survey and Mineral Exploration of Iran.

Lechmann A, Burg JP, Ulmer P, Guillong M and Faridi M (2018) Metasomatized mantle as the source of Mid-Miocene-Quaternary volcanism in NW-Iranian Azerbaijan: geochronological and geochemical evidence. *Lithos* **304**, 311–28.

Li JX, Qin KZ, Li GM, Xiao B, Chen L and Zhao JX (2011) Post collisional ore-bearing adakitic porphyries from Gangdese porphyry copper belt southern Tibet: Melting of thickened juvenile arc lower crust. *Lithos* **126**, 265–77.

Li L, Xiong XL and Liu XC (2017) Nb/Ta fractionation by amphibole in hydrous basaltic systems: implications for arc magma evolution and continental crust formation. *Journal of Petrology* **58**, 3–28.

Liu S, Hu RZ, Feng CX, Zhou HB, Li C, Chi XG, Peng JT, Zhong H, Qi L, Qi YQ and Wang T (2008) Cenozoic high Sr/Y volcanic rocks in the Qiangtang terrane northern Tibet: geochemical and isotopic evidence for the origin of delaminated lower continental melts. *Geological Magazine* **145**, 463–74.

Lohmeier S, Schneider A, Belyatsky B and Lehmann B (2019) Magmatic evolution of the Cerro Maricunga gold porphyry-epithermal system Maricunga belt N-Chile. *Journal of South American Earth Sciences* **92**, 374–99.

Ludwig KR (2012) *User's Manual for Isoplot 3.75-4.15. A Geochronological Toolkit for Microsoft Excel*. Berkeley: Berkeley Geochronology Center, Special Publication No. 5.

Luhr JF (1997) Extensional tectonics and the diverse primitive volcanic rocks in the western Mexican volcanic belt. *Canadian Mineralogist* **35**, 473–500.

MacPherson CG, Dreher ST. and Thirlwall MF (2006) Adakites without slab melting: high pressure differentiation of island arc magma Mindanao, the Philippines. *Earth and Planetary Science Letters* **243**, 581–93.

Martin H (1986) Effect of steeper Archaean geothermal gradient on geochemistry of subduction-zone magmas. *Geology* **14**, 753–756.

Martin H (1999) Adakitic magmas: modern analogues of Archaean granitoids. *Lithos* **46**, 411–429.

Martin H, Smithies RH, Rapp R, Moyen JF and Champion D (2005) An overview of adakite tonalite–trondhjemite–granodiorite (TTG) and sanukitoid: relationships and some implications for crustal evolution. *Lithos* **79**, 1–24.

Mohajjel M and Fergusson CL (2014) Jurassic to Cenozoic tectonics of the Zagros Orogen in the northwestern Iran. *International Geology Reviews* **56**, 263–287.

Mohajjel M, Fergusson CL and Sahandi MR (2003) Cretaceous–Tertiary convergence and continental collision Sanandaj–Sirjan Zone Western Iran. *Journal of Asian Earth Sciences* **21**, 397–412.

Mouthereau F, Lacombe O and Vergés J (2012) Building the Zagros collisional orogen: timing strain distribution and the dynamics of Arabia/Eurasia plate convergence. *Tectonophysics* **532**, 27–60.

Omrani H (2018) Island-arc and active continental margin adakites from the Sabzevar zone Iran. *Petrology* **26**, 96–113.

Omrani J, Agard P, Witechurch H, Benoit M, Prouteau G and Jolivet L (2008) Arc magmatism and subduction history beneath the Zagros Mountains Iran: a new report of adakites and geodynamic consequences. *Lithos* **106**, 380–98.

Paquette JL, Ménot RP, Pin C and Orsini JB (2003) Episodic and short-lived granitic pulses in a post-collisional setting: Evidence from precise U-Pb zircon dating through a crustal cross-section in Corsica. *Chemical Geology* **198**, 1–20.

Pearce JA, Harris NBW and Tindle AG (1984) Trace element discrimination diagram for the tectonic interpretation of granitic rock. *Journal of Petrology* **25**, 956–83.

Prouteau G, Scaillet B, Pichavant M and Maury R (2001) Evidence for mantle metasomatism by hydrous silicic melts derived from subducted oceanic crust. *Nature* **410**, 197–200.

Qin JF, Lai SC, Diwu CR, Ju YJ and Li YF (2010) Magma mixing origin for the post-collisional adakitic monzogranite of the Triassic Yangba pluton Northwestern margin of the South China block: geochemistry Sr-Nd isotopic zircon U-Pb dating and Hf isotopic evidences. *Contributions to Mineralogy and Petrology* **159**, 389–409.

Rabiee A, Rossetti F, Asahara Y, Azizi H, Lucci F, Lustrino M, Nozaem R, Lucci F, Lustrino M and Nozaem R (2020) Long-1 lived Eocene-Miocene stationary magmatism in NW Iran along a transform plate boundary. *Gondwana Research* **85**, 237–62.

Rapp RP, Shimizu N, Norman MD and Applegate GS (1999) Reaction between slab-derived melts and peridotite in the mantle wedge: experimental constraints at 3.8 GPa. *Chemical Geology* **160**, 335–56.

Rapp RP and Watson EB (1995) Dehydration melting of metabasalt at 8–32 kbar: implications for continental growth and crust–mantle recycling. *Journal of Petrology* **36**, 891–931.

Rapp RP, Watson EB and Miller CF (1991) Partial melting of amphibolite/ eclogite and the origin of Archean trondhjemites and tonalites. *Precambrian Research* **51**, 1–25.

Richards JP (2009) Postsubduction porphyry Cu–Au and epithermal Au deposits: products of remelting of subduction-modified lithosphere. *Geology* **37**, 247–50.

Richards JP, Spell T, Rameh E, Razique A and Fletcher T (2012) High Sr/Y magmas reflect arc maturity high magmatic water content and porphyry Cu ± Mo ± Au potential: Examples from the Tethyan arcs of Central and Eastern Iran and Western Pakistan. *Economic Geology* **107**, 295–332.

Richards JP, Wilkinson D and Ullrich T (2006) Geology of the Sari Gunay epithermal gold deposit northwest Iran. *Economic Geology* **101**, 1455–96.

Richards JR and Kerrich R (2007) Special paper: adakite-like rocks: their diverse origins and questionable role in metallogenesis. *Economic Geology* **102**, 537–76.

Rossetti F, Nasrabady M, Theye T, Gerdes A, Monié P, Lucci F and Vignaroli G (2014) Adakite differentiation and emplacement in a subduction channel: The late Paleocene Sabzevar magmatism (NE Iran). *GSA Bulletin* **126**, 317–43.

Sajona FG and Maury RC (1998) Association of adakites with gold and copper mineralization in the Philippines. *Comptes Rendus de l'Académie des Sciences Paris* **326**, 27–34.

Sajona FG, Maury R, Bellon H, Cotten J and Defant MJ (1996) High field strength element enrichment of Pliocene–Pleistocene island arc basalts Zamboanga Peninsula western Mindanao (Philippines). *Petrology* **37**, 693–716.

Schiano P, Clochiatti R, Shimizu N, Maury RC, Jochum KP and Hofman AW (1995) Hydrous silica-rich melts in the sub-arc mantle and their relationships with erupted arc lavas. *Nature* **377**, 595–600.

Shafaii Moghadam H, Li XH, Ling XX, Stern RJ, Santos JF, Meinhold G, Ghorbani Gh and Shahabi S (2015) Petrogenesis and tectonic implications of Late Carboniferous A-type and gabbronorites in NW Iran: Geochronological and geochemical constraints. *Lithos* **212–215**, 266–79.

Shafaii Moghadam H, Rossetti F, Lucci F, Chiaradia M, Gerdes A, Lopez Martinez M, Ghorbani G and Nasrabady M (2016) The calc-alkaline and adakitic volcanism of the Sabzevar structural zone (NE Iran): Implications for the Eocene magmatic flare-up in Central Iran. *Lithos* **248–251**, 517–35.

Shahbazi H, Siebel W, Ghorbani M, Pourmoafee M, Sepahi AA, Vousoughi Abedini M and Shang CK (2015) The Almogholagh pluton Sanandj-Sirjan

Zone Iran: geochemistry U-(Th)-Pb titanite geochronology and implication for its tectonic evolution. *Neues Jahrbuch für Mineralogie (Journal of Mineralogy and Geochemistry)* **192**, 85–99.

Shahbazi H, Siebel W, Pourmoafee M, Ghorbani M, Sepahi AA, Shang CK and Vousoughi Abedini M (2010) Geochemistry and U-Pb zircon geochronology of the Alvand plutonic complex in Sanandaj-Sirjan Zone (Iran): New evidence for Jurassic magmatism. *Journal of Asian Earth Sciences* **39**, 668–83.

Smithies RH (2000) The Archaean tonalite–trondhjemite–granodiorite (TTG) series is not an analogue of Cenozoic adakite. *Earth and Planetary Science Letters* **182**, 115–25.

Stampfli GM and Borel GD (2002) A plate tectonic model for the Paleozoic and Mesozoic constrained by dynamic plate boundaries and restored synthetic oceanic isochrones. *Earth and Planetary Science Letters* **196**, 17–33.

Stern CR and Kilian R (1996) Role of the subducted slab mantle wedge and continental crust in the generation of adakites from the Austral Volcanic Zone. *Contributions to Mineralogy and Petrology* **123**, 263–81.

Sun SS and McDonough WF (1989) Chemical and isotopic systematics of oceanic basalts: implications for mantle composition and processes. In *Magmatism in the Ocean Basins* (eds AD Saunders and MJ Norry), pp. 313–345. Geological Society of London, Special Publication no. **42**.

Tavakoli N, Davoudian AR, Shabanian N, Azizi H, Neubauer F, Asahara Y and Bernroider M (2020) Zircon U-Pb dating mineralogy and geochemical characteristics of the gabbro and gabbro-diorite bodies Boein–Miandasht western Iran. *International Geology Review* **62**, 1658–76.

Torkian A, Furman T, Salehi N and Veloski K (2019) Petrogenesis of adakites from the Sheyda volcano NW Iran. *Journal of African Earth Sciences* **150**, 194–204.

Veysi S, Asiabanha A, Shahbazi H and Nasrabadi M (2015) Enclaves in the scoria cone of the Qezeljeh-Kand (N-Ghorveh): xenolith or cumulate? *Iranian Journal of Geology* **9**, 51–70 (in Farsi).

Wang Q, Xu JF, Jian P, Bao ZW, Zhao ZH, Li CF, Xiong XL and Ma JL (2006) Petrogenesis of adakitic porphyries in an extentional tectonic setting Dexing South China: implications for the genesis of porphyry copper mineralization. *Journal of Petrology* **47**, 119–44.

Whitney DL and Evans BW (2010) Abbreviations for names of rock-forming minerals. *American Mineralogist* **95**, 185–87.

Wiedenbeck M, Hanchar JM, Peck WH, Sylvester P, Valley J, Whitehouse M, Kronz A, Morishita Y, Nasdala L, Fiebig J and Franchi I (2004) Further characterisation of the 91500 zircon crystal. *Geostandards and Geoanalytical Research* **28**, 9–39.

Wilkinson DL (2005) Geology and mineralisation of the Sari Gunay gold deposits Kordestan province Iran. Tehran: Geology and Mineralisation Study Report, Zar Kuh Mining Company, Iran, 86 p.

Winchester J and Floyd P (1977) Geochemical discrimination of different magma series and their differentiation products using immobile elements. *Chemical Geology* **20**, 325–43.

Wolf MB and Wyllie PJ (1994) Dehydration-melting of amphibolite at 10 kbar: the effects of temperature and time. *Contributions to Mineralogy and Petrology* **115**, 369–83.

Zhu DC, Zhao ZD, Pan GT, Lee HY, Kang ZQ, Liao ZL, Wang LQ, Li GM, Dong GC and Liu B (2009) Early Cretaceous subduction-related adakite-like rocks of the Gangdese Belt southern Tibet: products of slab melting and subsequent melt peridotite interaction? *Journal of Asian Earth Sciences* **34**, 298–309.